

# 1 IL-6 blockade suppresses the blood–brain barrier disorder, 2 leading to prevention of onset of NMOSD

3 **Authors:** Yukio Takeshita<sup>1†</sup>, Susumu Fujikawa<sup>1†</sup>, Kenichi Serizawa<sup>2</sup>, Miwako Fujisawa<sup>1</sup>, Kinya Matsuo<sup>1</sup>,  
4 Joe Nemoto<sup>1</sup>, Fumitaka Shimizu<sup>1</sup>, Yasuteru Sano<sup>1</sup>, Haruna Tomizawa-Shinohara<sup>2</sup>, Shota Miyake<sup>2</sup>,  
5 Richard M. Ransohoff<sup>3</sup>, Takashi Kanda<sup>1\*</sup>

6 **Affiliations:**

7 <sup>1</sup>Department of Neurology and Clinical Neuroscience, Yamaguchi University Graduate School of Medicine,  
8 Yamaguchi, Japan.

9 <sup>2</sup>Product Research Department, Chugai Pharmaceutical Co., Ltd, Kanagawa, Japan.

10 <sup>3</sup>Third Rock Ventures, Boston, USA

11 **\*Corresponding author:** Email: tkanda@yamaguchi-u.ac.jp

12 <sup>†</sup>These authors contributed equally to this work.

13 **One sentence summary:** Satalizumab and IL-6 blockade prevent lymphocyte migration and barrier  
14 dysfunction induced by NMO-IgG in EAE and novel triple co-culture BBB models.

15 **Running title:** IL-6 blockade suppress the BBB disorder

16

17 **Abstract:** Neuromyelitis optica spectrum disorder (NMOSD) is an autoimmune astrocytopathy caused by  
18 antibodies against the aquaporin 4(AQP4) in end-feet of astrocytes. Breakdown of the blood–brain barrier  
19 (BBB) allowing ingress of AQP4 antibodies into the central nervous system (CNS) plays a key role in  
20 NMOSD. Although IL-6 blockade therapies such as satralizumab are effective in NMOSD, the therapeutic  
21 mechanism of IL-6 blockade, especially with respect to BBB disruption, are not fully understood because of  
22 the lack of the human models that are specialized to evaluate the BBB function.  
23 We constructed new in vitro human BBB models for evaluating continued barrier function, leukocyte  
24 transmigration and intracerebral transferability of IgGs utilizing the newly established triple co-culture system.  
25 In vitro and vivo experiments revealed that NMO-IgG increased intracerebral transferability of satralizumab,  
26 and that satralizumab suppressed the NMO-IgG-induced transmigration of T cells and barrier dysfunction.  
27 These results suggest that satralizumab, which can pass through the BBB in the presence of NMO-IgG,  
28 suppresses the barrier dysfunction and the disrupting controlled cellular infiltration at the BBB, leading to  
29 prevention of onset of NMOSD.

## 30      **Introduction**

31      Neuromyelitis optica spectrum disorder (NMOSD) is an inflammatory disease of the central nervous system  
32      (CNS) associated with recurrent optic neuritis and longitudinally extensive transverse myelitis (1, 2). A major  
33      characteristic of NMOSD is the development of antibodies against the water channel aquaporin-4 (AQP4),  
34      which is expressed mainly in astrocytic foot processes (3, 4). The IgG plasma fraction of NMOSD patients  
35      (NMO-IgG) contains anti-AQP4 antibodies, leading to complement- and antibody-dependent cellular  
36      cytotoxicity of astrocytes (5–7). In order for peripherally produced anti-AQP4 antibodies to gain access to their  
37      target in the CNS, they need to penetrate the blood–brain barrier (BBB) (8). Accordingly, disruption of the  
38      BBB—which allows influx of humoral factors including autoantibodies through the dysfunctional barrier and  
39      infiltration of inflammatory cells by disruption of controlled cellular infiltration—is considered to be the first  
40      and key step in the pathogenesis of NMOSD (9–11). In fact, the ratio of cerebrospinal fluid (CSF) to serum  
41      albumin (CSF:serum albumin ratio), which is a marker of BBB permeability, is correlated with the clinical  
42      severity of NMOSD (12, 13).

43      Levels of interleukin-6 (IL-6) are elevated in the CSF and serum of patients with NMOSD as compared  
44      with levels in patients with multiple sclerosis or non-inflammatory neurologic disease (14–16). In earlier  
45      studies (11, 17), we found that anti-GRP78 and anti-AQP4 autoantibodies in NMO-IgG were important factors  
46      in the breakdown of the BBB via induction of IL-6 expression in astrocytes. In recent *ex-vivo* experiments,  
47      inhibition of IL-6 signaling was shown to inactivate the effector functions of plasmablasts, which are a major  
48      source of NMO-IgG in the peripheral blood (18). In terms of BBB disruption, IL-6 dose- and time-dependently  
49      decreases the expression of endothelial tight junction proteins and increases permeability in human brain  
50      microvascular endothelial cells (19). In patients with NMOSD, increased IL-6 in the CSF is positively  
51      correlated with the CSF:serum albumin ratio (20). Overall, these reports suggest that IL-6 signaling pathways  
52      are involved in the pathogenesis of NMOSD. In fact, clinical research has demonstrated that treatment with  
53      anti-IL-6 receptor antibody ameliorates the disease in patients with NMOSD (21, 22).

54      Satralizumab is a humanized immunoglobulin G subclass 2 (IgG2) monoclonal antibody against IL-6  
55      receptors; it specifically binds to both membrane-bound and soluble forms of IL-6 receptors and blockades IL-

56 6 signaling pathways (23). The constant and variable regions of satralizumab are engineered to have pH-  
57 dependent binding to IL-6 receptors, increased affinity to the neonatal Fc receptor, and a lower isoelectric  
58 point to extend the elimination half-life of the drug in plasma (24, 25). Importantly, it is reported that  
59 satralizumab showed beneficial effects such as a lower risk of relapse than with placebo among patients with  
60 NMOSD in an international, randomized, double-blind, placebo-controlled, phase 3 trial (26). However, the  
61 therapeutic mechanisms of satralizumab, especially those with respect to BBB disruption, still remain  
62 unknown because there are no ideal *in vivo* or *in vitro* BBB models with which to explore NMOSD  
63 pathogenesis.

64 To address this pertinent issue, we propose some important properties that will be necessary for an *in vitro*  
65 BBB model that is more robust than those currently available (27). First, the model should include human cells  
66 that maintain both physiological and morphological BBB properties *in vitro*. Second, endothelial cells should  
67 be co-cultured with other BBB cells such as astrocytes and pericytes. Third, the model should allow the  
68 transendothelial migration of inflammatory cells under physiologically relevant shear forces. Additionally, the  
69 model should allow recovery of transmigrated cells for further analysis of BBB function, including real-time  
70 monitoring of transendothelial electrical resistance (TEER) and the measurement of microvolumes of humoral  
71 factors or IgG translocation across the BBB.

72 In order to construct *in vitro* BBB models with these properties, we utilized human brain microvascular  
73 endothelial cells (hECs; TY10), human astrocytes (hASTs) with AQP4 expression, and human pericytes  
74 (hPCTs), each of which was conditionally immortalized by transfection with temperature-sensitive SV40  
75 (simian virus 40) large T antigen (ts-SV40-LT) and which retain both their physiological and morphological  
76 BBB properties (28, 29). We earlier constructed a flow-based *ex-vivo* models of hECs co-cultured with hASTs  
77 that enables us to evaluate the transmigration of leukocytes across the endothelium under shear  
78 forces (11, 30, 31). However there were no ideal triple co-cultured *in vitro* and *ex-vivo* BBB model in which  
79 pericytes and the end-feet of astrocytes can directly contact endothelial cells. Then it was impossible to  
80 evaluate the barrier function, leukocyte transmigration and intracerebral transferability to reveal NMOSD  
81 pathogenesis

82 In the present study, we constructed functional *in vitro* static and *in ex-vivo* flow-based models utilizing  
83 the newly established triple co-culture system of temperature-sensitive conditionally immortalized human  
84 BBB cell lines (endothelial cells [hECs], pericytes [hPCTs], and astrocytes with AQP4 expression [hASTs]) in  
85 order to explore the effects of NMO-IgG on the BBB. The new static *in vitro* model allowed long-term  
86 measurement of real-time TEER by means of an automated cell monitoring system and measurement of  
87 microvolumes of IgG translocation through the BBB. The new *in ex-vivo* flow-based model enabled us to  
88 evaluate leukocyte transmigration across the BBB. Then, using these structured *in vitro* BBB models, we  
89 evaluated the effects of satralizumab on BBB disruption caused by NMO-IgG. In addition to the *in vitro*  
90 assays, we also assessed the effects of an anti-IL-6 receptor antibody for mice (MR16-1) on *in vivo* BBB  
91 disruption in mice with experimental autoimmune encephalomyelitis (EAE). These mice are used as an animal  
92 model of CNS autoimmune diseases in which IL-6 concentration in the spinal cord dramatically increases (32).

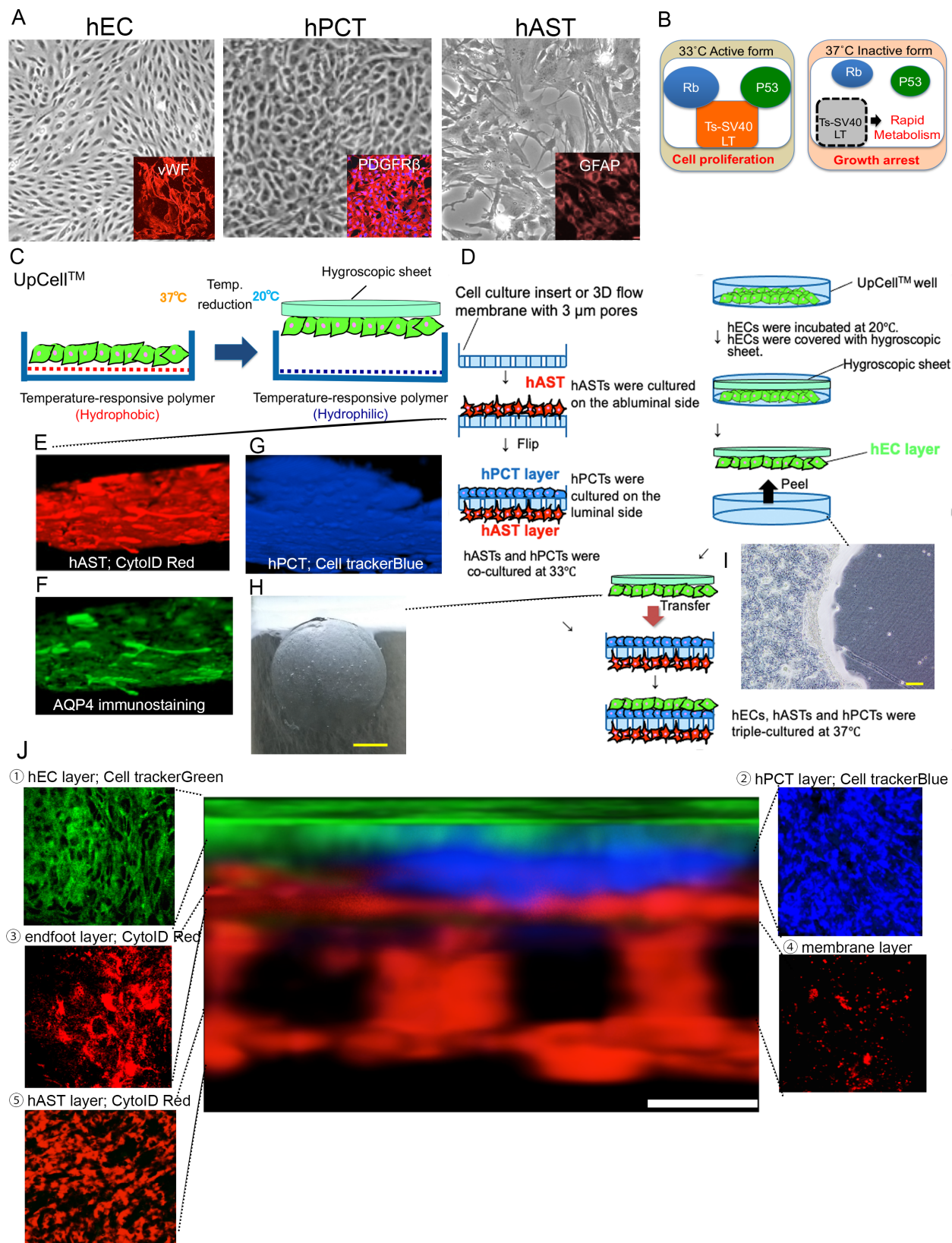
## 93 **Results**

94

### 95 ***Construction newly in vitro BBB models with triple co-culture system of temperature-sensitive*** 96 ***conditionally immortalized human BBB cell lines.***

97 We utilized human brain microvascular endothelial cells (hECs; TY10), human astrocytes (hASTs) with  
98 AQP4 expression, and human pericytes (hPCTs), each of which was conditionally immortalized by  
99 transfection with temperature-sensitive SV40 (simian virus 40) large T antigen (ts-SV40-LT) and which retain  
100 both their physiological and morphological BBB properties(Fig.1A). In transfected these cell lines, cells are  
101 driven to continue proliferating at 33°C because activated Ts-SV40 LT inhibited P53 and Rb. On the other  
102 hand, cells could differentiate into mature cells at 37 °C because Ts-SV40 LT is inactivated and exhibit growth  
103 arrest (Fig.1 B). To construct triple co-culture systems of these temperature-sensitive conditionally  
104 immortalized human BBB cell lines, multiple steps were organized by including cell-culture on Upcell dish  
105 with coated temperature-responsive polymer (Fig. C and D). Firstly, hASTs were cultured on abluminal side of  
106 insert membranes having 3  $\mu$ m pores and incubated for 24 hours so that some astrocytic end-feet with AQP4  
107 could protrude through the membrane pores (Fig.1 E and F). Secondly, after culturing of hPCTs on the

108 luminal side of membranes (Fig.1 G), hASTs and hPCTs were co-cultured at 33 °C for 24 hours. Thirdly,  
109 hECs were cultured on Upcell dish with coated temperature-responsive polymer, which can achieve sheet-like  
110 detachment of confluent cells and extra-cellular matrix by temperature-shifting to 20°C (Fig.1 I and H). Then  
111 sheet-like detachment of confluent hEC were transferred onto the hPCTs. After co-cultuting of these cell lines  
112 at 33 °C for 24 hours, they differentiated into mature cells under the condition of 37 °C. Confocal 3D analysis  
113 with living staining of each cell line showed that multi-cultured insert constituted the five-layer structures  
114 which is consisted of hEC, hPCT, astrocytic endfeet, membrane, and hAST(Fig.1 J 1-5). Some end-feet  
115 protruded through the membrane pores. hPCTs and end-feet of hASTs were close to the hEC layer.



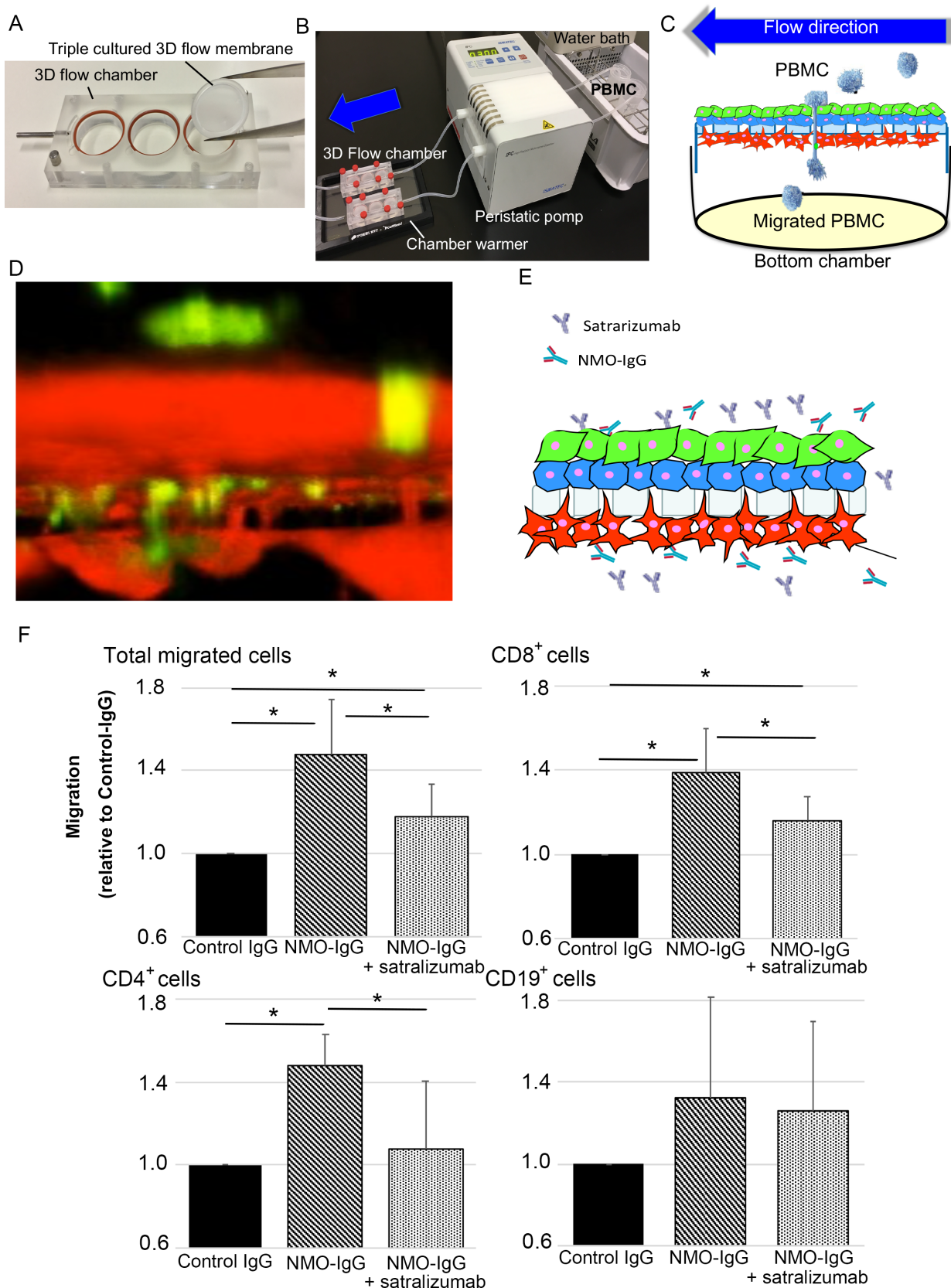
117 Figure 1  
118 Construction newly *in vitro* BBB model with triple co-culture system of temperature-sensitive conditionally  
119 immortalized human BBB cell lines.  
120 A) Establishment of the BBB cell lines that maintains the BBB properties. Morphology of hEC is spindle-  
121 shape. hEC expressed vWF as lineage marker of endothelium. Morphology of hPCT is cobblestone-shape.  
122 hPCT expressed PDGF $\beta$  as lineage marker of pericyte. Morphology of hAST is star-shape. hAST expressed  
123 GFAP as lineage marker of hAST. B) Three conditionally immortalized human cell lines were transfected with  
124 temperature sensitive SV40 large T antigen (Ts-SV40 LT). At 33°C, activated Ts-SV40 LT binds and inhibits  
125 p53 and Rb, which are strong tumor suppressors, leading to continuous cell proliferation. At 37 °C, inactivated  
126 Ts-SV40 LT exhibit growth arrest, leading to differentiate into mature cells. C) The UpCell<sup>TM</sup> technology.  
127 Temperature-responsive polymer is immobilized on the surface of UpCell<sup>TM</sup> well. The polymer grafted surface  
128 shows reversible hydrophobic - hydrophilic property across the threshold temperature of 32°C, cell-sheet is  
129 detached from the dish without harmful enzymes (e.g. trypsin or dispase) and attached the hygroscopic sheet to  
130 transfer. D) Multistep of triple co-culture system. hASTs were cultured on the abluminal side of cell culture  
131 insert or 3D flow membrane with 3 $\mu$ m pores. After flipping of cultured insert, hPCTs were cultured on the  
132 luminal side. hAST and hPCTs were co-cultured at 33°C. hEC were cultured on UpCell dish. After incubation  
133 at 20°C, The sheet of confluent hECs was detached and transferred onto the hPCTs co-cultured with hASTs on  
134 the insert. E,F) Astrocytic endfoot with AQP4 on cultured membrane. living-stained hAST cultured on  
135 membrane. Confocal 3D analysis from luminal side of membrane with living staining of hAST(E) and  
136 immunostaining of AQP4(F) showed some astrocytic end-feet protruded through the membrane pores. G)  
137 hPCT were co-cultured on the luminal side of the membrane. Confocal 3D analysis from luminal side of  
138 membrane with living staining of hPCT showed hPCT layer was on the membrane without any tentacles like  
139 astrocytic end-feet. H-I) Sheet-like detachment (H) and traces of peeling on dish of confluent hECs (I). H, bar  
140 = 200  $\mu$ m. I, bar= 10 mm. J) Confocal 3D analysis with living staining of each cell lines. Multi-cultured insert  
141 constituted the five-layer structures which is consisted of hEC, hPCT, astrocytic endfeet, membrane, and hAST  
142 (1-5). Some end-feet protruded through the membrane pores. hPCTs and end-feet of hASTs were close to the  
143 hEC layer. bar = 5  $\mu$ m

144

145 ***Construction of ex vivo BBB model with triple co-culture system for leukocyte transmigration***  
146 ***and effect of satralizumab on NMO-IgG-induced transmigration of leukocytes in ex-vivo.***

147 To evaluate the effect of satralizumab on NMO-IgG-induced transmigration of leukocytes, we constructed a  
148 flow-based dynamic BBB model incorporating hEC/hPCT/hAST triple co-culture, which allows further

149 investigation of leukocyte transmigration under flow (Fig.2 A-D). After exposing the endothelial cell side  
150 (vascular side) and the astrocyte side (brain parenchymal side) to satralizumab plus NMO-IgG or to NMO-IgG  
151 alone (Fig.2. E), we counted the total numbers of all migrating cells and the numbers of phenotyped cells and  
152 compared their migrations relative to those with Control IgG. Application of NMO-IgG increased the  
153 migrations of all peripheral blood mononuclear cells (PBMCs) and CD4<sup>+</sup>, CD8<sup>+</sup>, and CD19<sup>+</sup> cells relative to  
154 their migrations with Control IgG, and the application of NMO-IgG plus satralizumab significantly suppressed  
155 this increase in the relative numbers of migrating PBMCs and CD4<sup>+</sup> and CD8<sup>+</sup> cells (Fig. 2 F).



157 **Figure 2**

158 **Construction of *ex-vivo* BBB model with triple co-culture system for leukocyte transmigration and**  
159 **effect of satralizumab on NMO-IgG-induced transmigration of leukocytes *in ex-vivo*.**

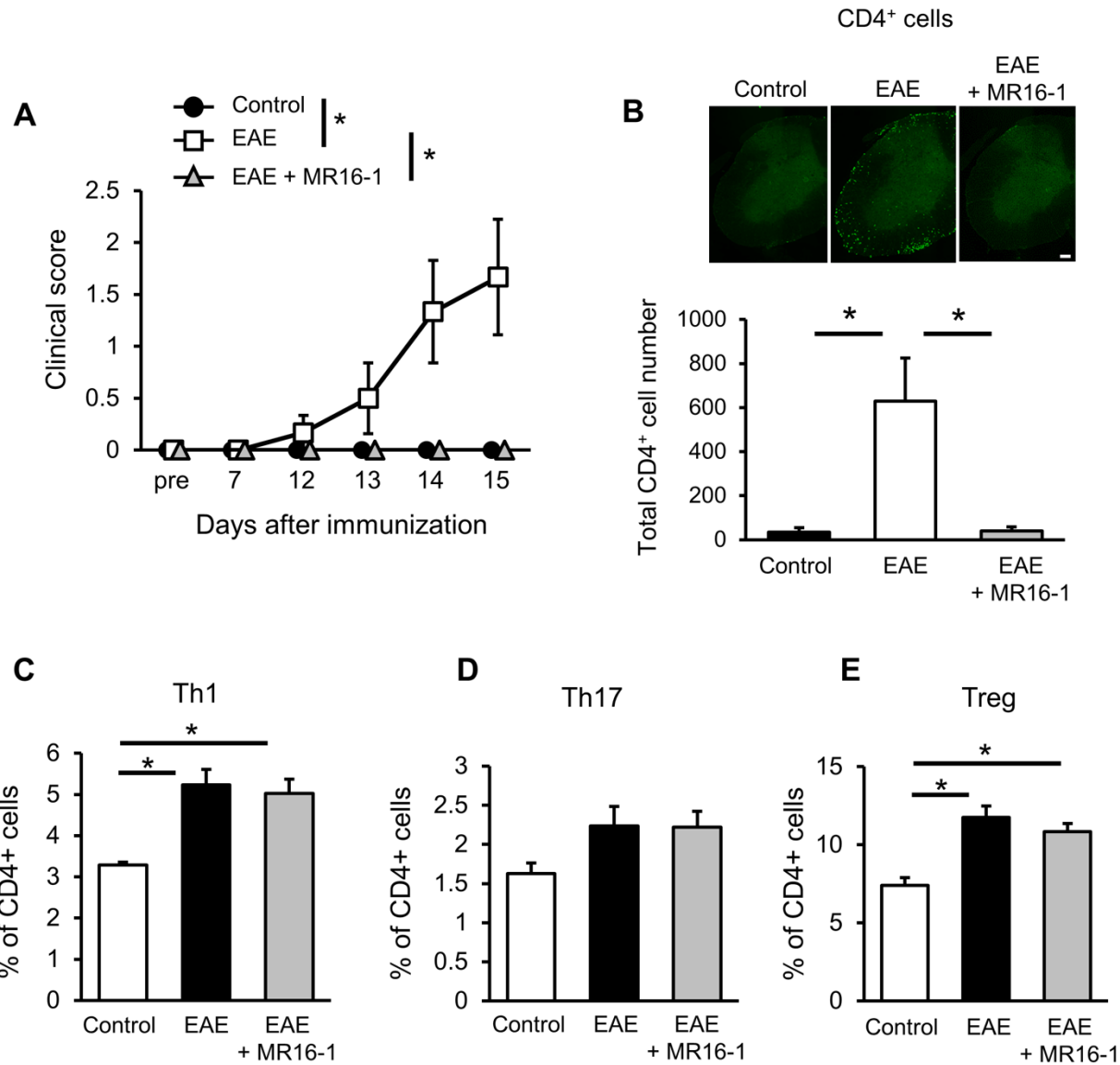
160 A) 3D flow chamber and 3D flow membrane. the triple-cultured membranes were transferred in 3D chamber.  
161 B) Whole set up of migration assay under shear forces. Normal human peripheral blood mononuclear cells  
162 (PBMC) flowed onto luminal side with physiological shear force by peristatic pomp. C) Schema of 3D flow  
163 chamber in transmigration assay. Total migrated cells were recovered from the bottom chamber and  
164 enumerated. D) Confocal 3D analysis with living staining of BBB cell lines and PBMCs in transmigration  
165 assay. PBMC were stained with Cell trackerGreen and all human BBB cell lines (hECs, hPCTs, and  
166 hASTs) were stained with CytoID Red. Some PBMCs protruded through the membrane pores. E)  
167 Schema of leukocyte transmigration assay with NMO-IgG and/or Satralizumab. F) Flow-based leukocyte  
168 transmigration assays utilizing a 3D flow Chamber showed that application of NMO-IgG increased the  
169 numbers of total migrating PBMCs and CD4<sup>+</sup>, CD8<sup>+</sup>, and CD19<sup>+</sup> cells relative to numbers migrating with  
170 Control IgG, and that the application of NMO-IgG plus satralizumab significantly suppressed that increase. \**P*  
171 < 0.05 by unpaired t-test (*n* = 6 per group). All data are expressed as mean and SEM.

172

173 **Effects of IL-6 receptor blockade on clinical signs and on transmigration of leukocytes in**  
174 **EAE mice**

175 Administration of MR16-1 (anti-IL-6 receptor antibody for mice) on Day 7 after induction of experimental  
176 autoimmune encephalomyelitis significantly and strongly prevented the onset of clinical signs in EAE mice  
177 (Fig. 3A). We then confirmed the effect of MR16-1 on leukocyte transmigration in EAE mice. On Day 15, the  
178 number of CD4<sup>+</sup> T cells markedly increased in the spinal cords of EAE mice, whereas these cells were almost  
179 undetected in the spinal cords of Control mice (Control,  $33.7 \pm 21.5$  [mean  $\pm$  SEM] cells/spinal cord slice;  
180 EAE,  $628.3 \pm 196.5$  cells/spinal cord slice) (Fig. 3B). Administration of MR16-1 on Day 7 significantly  
181 prevented the migration of CD4<sup>+</sup> T cells into the spinal cord (EAE + MR16-1,  $40.3 \pm 17.7$  cells/spinal cord  
182 slice) (Fig. 3B). To exclude the possibility that the impact of MR16-1 on clinical signs and on leukocyte  
183 migration into the spinal cord was secondary to changes in the immune response, we evaluated the effect of  
184 MR16-1 on T cell differentiation in EAE mice. In splenocytes, Th1 cells and FoxP3-positive regulatory T cells  
185 were significantly increased on Day 16 in EAE mice (Fig. 3, C and E). Th17 cells showed a tendency, but not

186 significantly, to increase in EAE mice (Fig. 3D). Administration of anti-IL-6 receptor antibody on Day 7 did  
187 not affect the induction of these in EAE mice (Fig. 3, C to E).



188

189

190 **Figure 3.**

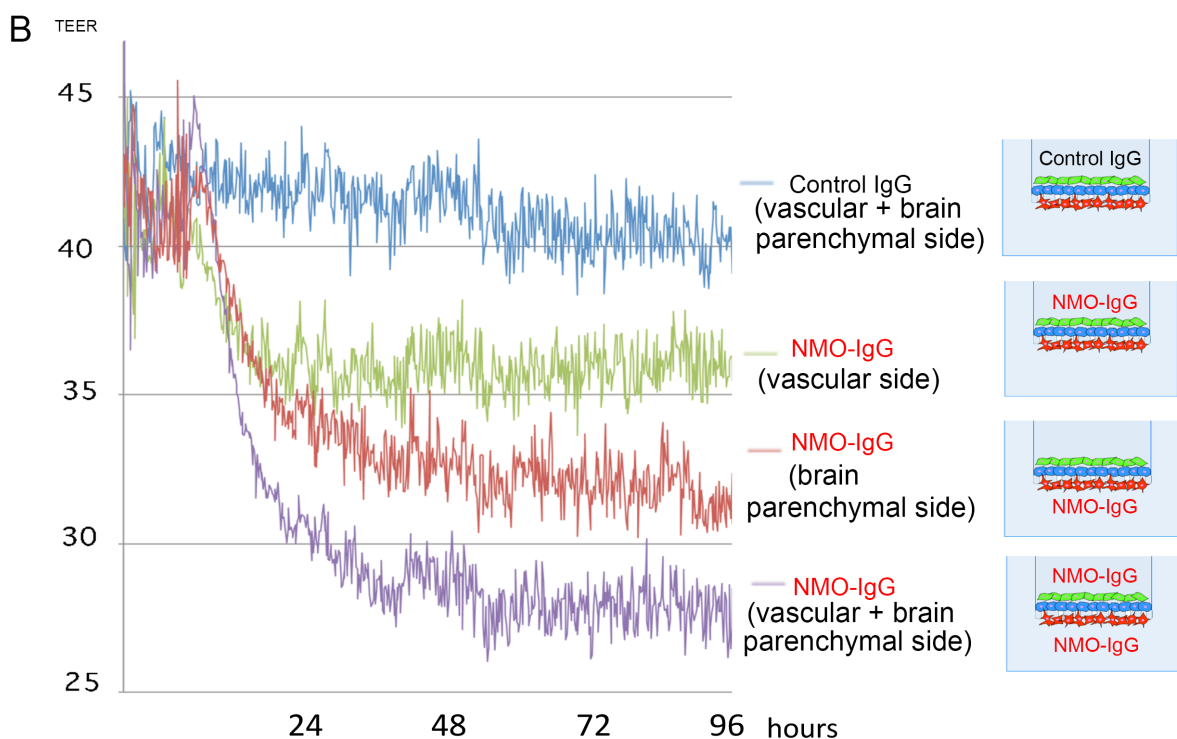
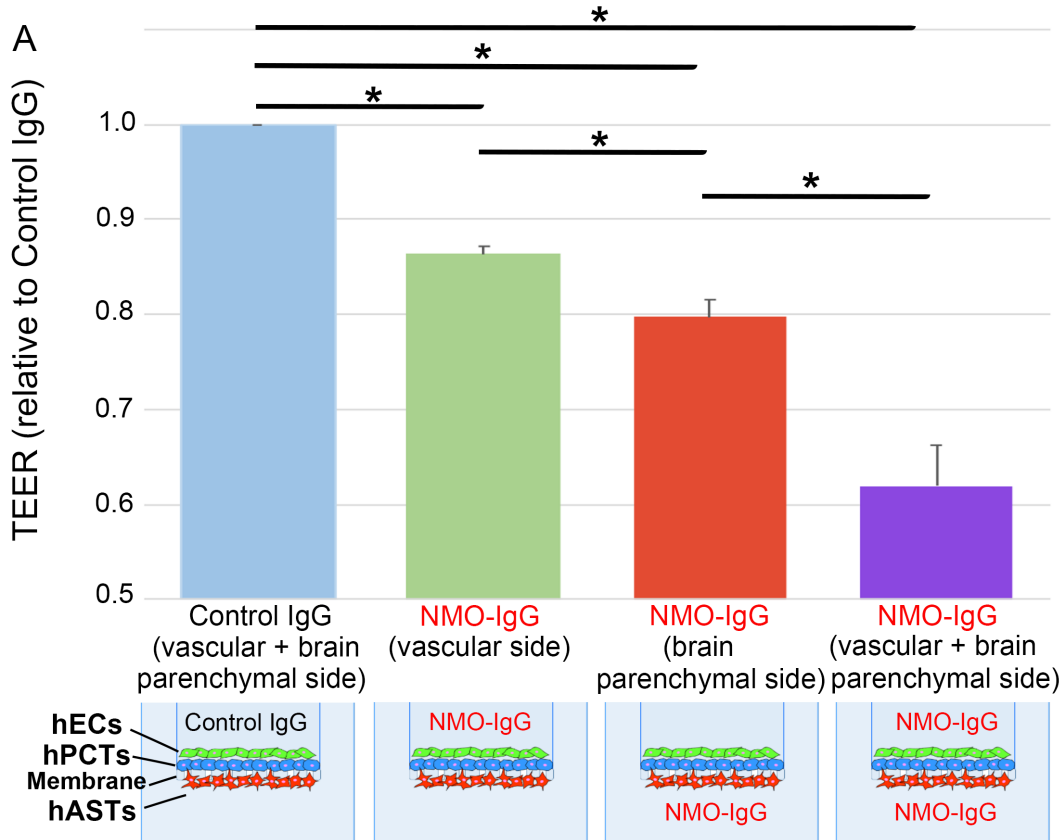
191 **Effects of IL-6 receptor blockade on lymphocyte migration into the spinal cord *in vivo*.**

192 (A) Anti-IL-6 receptor antibody (MR16-1) was administered on Day 7 after immunization. Anti-IL-6 receptor  
193 antibody significantly prevented the onset of clinical signs in EAE mice. \* $P < 0.05$  by two-way ANOVA ( $n =$   
194 3–6 per group). (B) Anti-IL-6 receptor antibody suppressed lymphocyte migration into the spinal cords of EAE  
195 mice. Representative images showing immunohistochemical staining for CD4<sup>+</sup> cells in the spinal cord on Day  
196 15 after immunization. The number of CD4<sup>+</sup> T cells was markedly increased in the spinal cord of EAE mice.  
197 Anti-IL-6 receptor antibody administered on Day 7 after immunization significantly prevented this increase.  
198 \* $P < 0.05$  by Tukey's multiple comparison test ( $n = 3–6$  per group). Scale bar = 100  $\mu$ m. (C) The induction of  
199 Th1 cells and (E) FoxP3-positive regulatory T cells was significantly upregulated on Day 16 after  
200 immunization. There was a tendency, but not significantly, for Th17 cells to increase in EAE mice (D).  
201 Administration of anti-IL-6 receptor antibody on Day 7 after immunization did not change the induction of  
202 these in EAE mice. \*  $P < 0.05$  by Tukey's multiple comparison test ( $n = 4–8$  per group). All data are expressed  
203 as mean and SEM.

204

205 **Damage to the barrier function of the BBB by NMO-IgG *in vitro***

206 To evaluate whether NMO-IgG affects the barrier function of the BBB on the vascular side or the brain  
207 parenchymal side, we constructed the static *in vitro* BBB model which allowed long-term measurement of  
208 real-time TEER by means of an automated cell monitoring system. After addition of NMO-IgG or Control IgG  
209 with either the vascular side, the brain parenchymal side, or both sides, the TEER values were measured by  
210 using an automated cell monitoring device that recorded the TEER value every minute for 5 consecutive days.  
211 Within 24 hours of application of NMO-IgG, TEER values in all groups had begun to decrease compared to  
212 Control IgG, and at 72 hours they had significantly decreased in all groups (Fig. 4, A and B). Application of  
213 NMO-IgG to both the vascular and brain parenchymal sides resulted in the lowest TEER values of all groups.  
214 TEER values with brain parenchymal application of NMO-IgG were significantly lower than TEER values  
215 with vascular application of NMO-IgG.



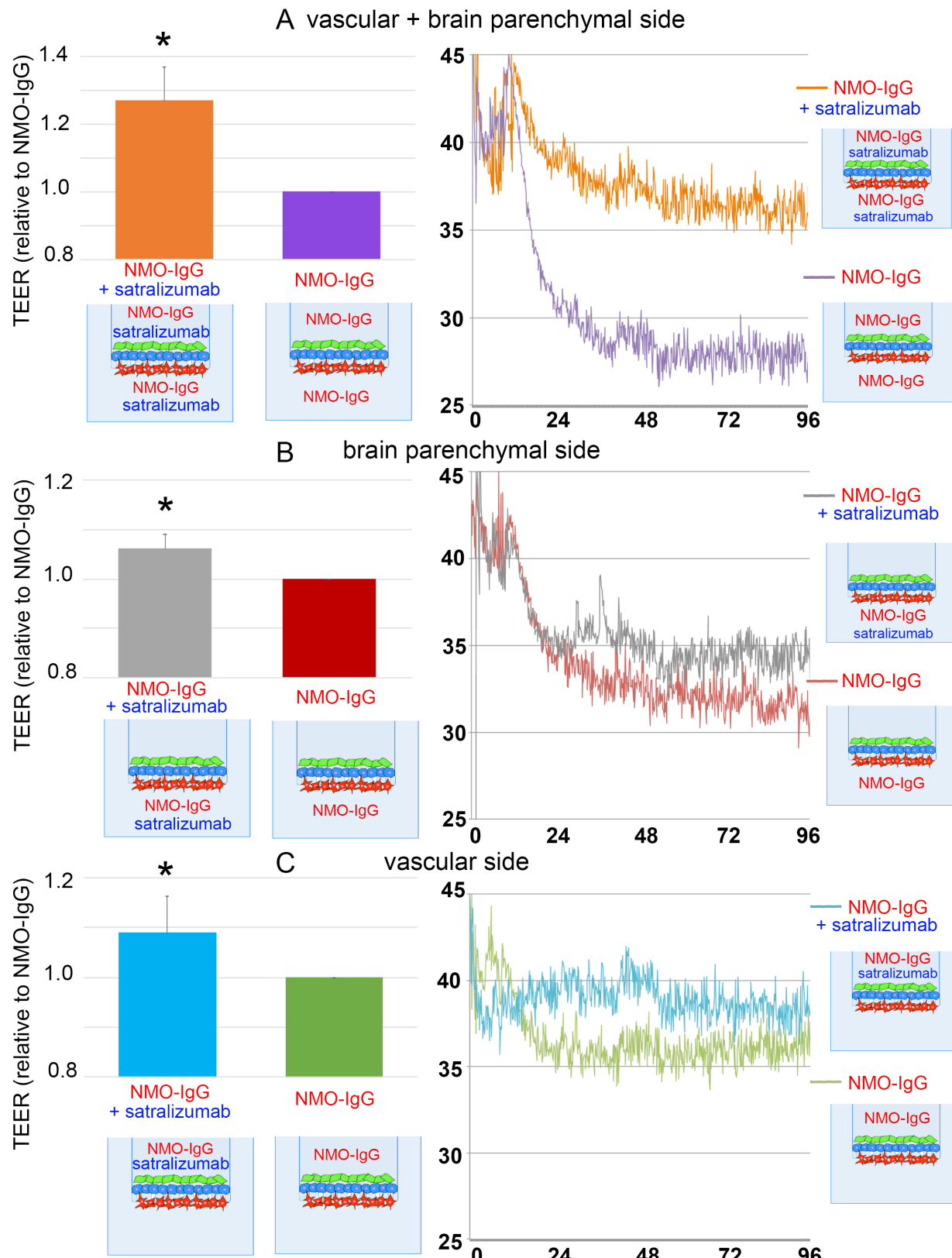
217 **Figure 4. Damage to the barrier function of the BBB by NMO-IgG in vitro.**

218 (6) Application of NMO-IgG to either the vascular side or the brain parenchymal side or both sides of the  
219 static BBB model significantly decreased the TEER value relative to that of Control IgG at 72 hours. \* $P <$   
220 0.05 by unpaired t-test ( $n = 3$  per group). All data are expressed as mean and SEM. (B) Real-time TEER  
221 measurement by cellZscope showed that the TEER values had started to decrease within 24 hours of  
222 application of NMO-IgG in all groups, and the declining trend continued for 48 hours.

223

224 ***Effects of satralizumab on the barrier function of the BBB in vitro***

225 To evaluate whether satralizumab affects the BBB dysfunction induced by NMO-IgG, we used the static  
226 *in vitro* BBB model incorporating hEC/hPCT/hAST triple co-culture with either the vascular side or the brain  
227 parenchymal side or both sides exposed to NMO-IgG. After addition of satralizumab plus NMO-IgG or  
228 Control IgG to either the vascular side or the brain parenchymal side or both sides, TEER values were  
229 measured by the automated cell monitoring device as mentioned above. TEER values at 72 hours were  
230 significantly higher under conditions where both the vascular side and the brain parenchymal side were  
231 exposed to satralizumab plus NMO-IgG, than under conditions of NMO-IgG alone (Fig. 5A). The inhibiting  
232 effect of satralizumab on barrier dysfunction was almost the same when satralizumab was applied to the brain  
233 parenchymal side as it was when applied to the vascular side (Fig. 5, B and C). Application of satralizumab to  
234 both the vascular and brain parenchymal sides had the highest inhibiting effect on barrier dysfunction among  
235 the three conditions (Fig. 5, A to C).



237 **Figure 5.**

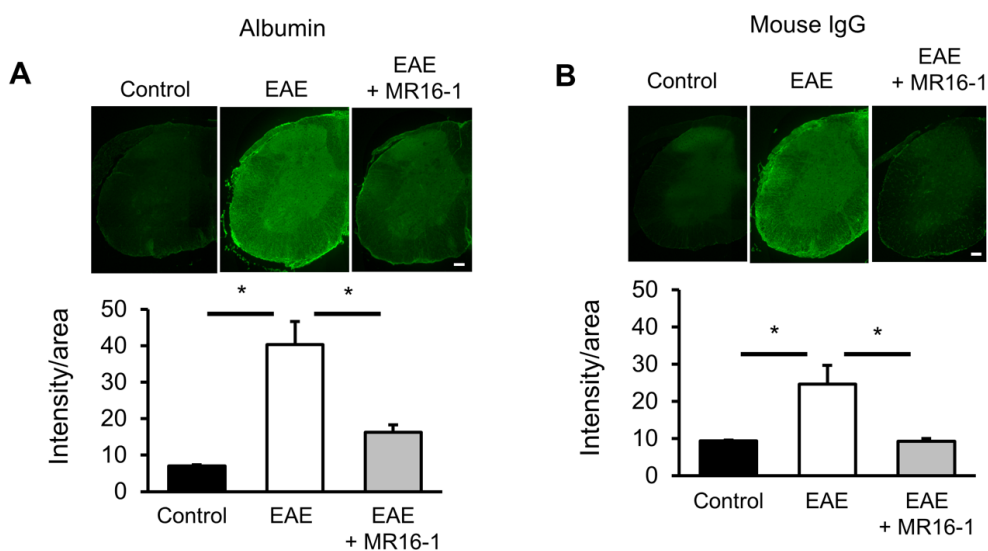
238 **Effects of satralizumab on the barrier function of the BBB in vitro. (A to C, left panels)**

239 After addition of satralizumab and NMO-IgG to either the vascular side or the brain parenchymal side or both  
240 sides, the TEER values under conditions of satralizumab plus NMO-IgG were significantly higher than under  
241 conditions of NMO-IgG alone at 72 hours. \* $P < 0.05$  by unpaired t-test ( $n = 3$  per group). All data are  
242 expressed as mean and SEM. (A to C, right panels) Real-time TEER measurement by cellZscope showed a  
243 declining trend in TEER values under conditions of satralizumab plus NMO-IgG in all groups, but the decline  
244 remained less than that for NMO-IgG alone for 96 hours.

245

246 **Effects of IL-6 receptor blockade on the barrier function of the BBB in EAE mice**

247 Immunohistochemical analysis on Day 15 showed that leakage of albumin and IgG into the spinal cord was  
248 higher in EAE mice than in Control mice (Fig. 6, A and B). This leakage into the CNS indicates the increased  
249 permeability of the BBB. Treatment of EAE mice with MR16-1 significantly prevented these leakages into the  
250 spinal cord. As regards the inhibiting effect on barrier dysfunction with application of satralizumab on the  
251 vascular side, we showed that sera from EAE mice mildly reduced the barrier function of endothelial cells in  
252 monoculture (Fig. S1) Serum from EAE mice at onset of EAE on Day 16 after immunization significantly  
253 decreased the TEER value of a monolayer of mouse primary BMECs. Anti-IL-6 receptor antibody  
254 significantly prevented this reduction.



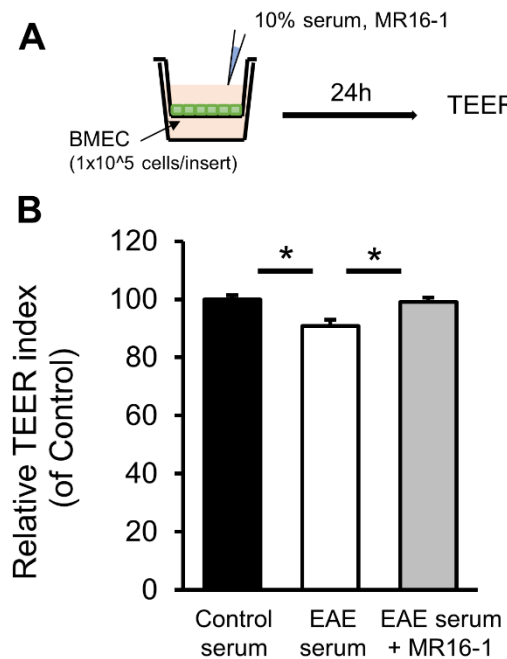
255

256

257 **Figure 6**

258 **Effects of IL-6 receptor blockade on BBB permeability *in vivo*. (A and B)**

259 Representative images showing immunohistochemical staining for albumin (A) and IgG (B) in the spinal cord  
260 on Day 15 after immunization. Leakage of albumin and IgG into the spinal cord was higher in EAE mice than  
261 in Control mice, and was significantly reduced by treatment with anti-IL-6 receptor antibody (MR16-1). \* $P <$   
262 0.05 by Tukey's multiple comparison test ( $n = 3-6$  per group). Scale bars = 100  $\mu$ m. All data are expressed as  
263 mean and SEM.



264

265 **Fig. S1. Effects of IL-6 receptor blockade on the barrier dysfunction induced by serum from EAE mice.**  
266 (A) Graphical representation of study design used to evaluate the effect of anti-IL-6 receptor antibody on the  
267 TEER of brain microvascular endothelial cells (BMECs). (B) Serum from EAE mice at onset of EAE on Day  
268 16 after immunization significantly decreased the TEER value of a monolayer of mouse primary BMECs.  
269 Anti-IL-6 receptor antibody significantly prevented this reduction. \* $P < 0.05$  by Tukey's multiple comparison  
270 test ( $n = 8$  per group). All data are expressed as mean and SEM.

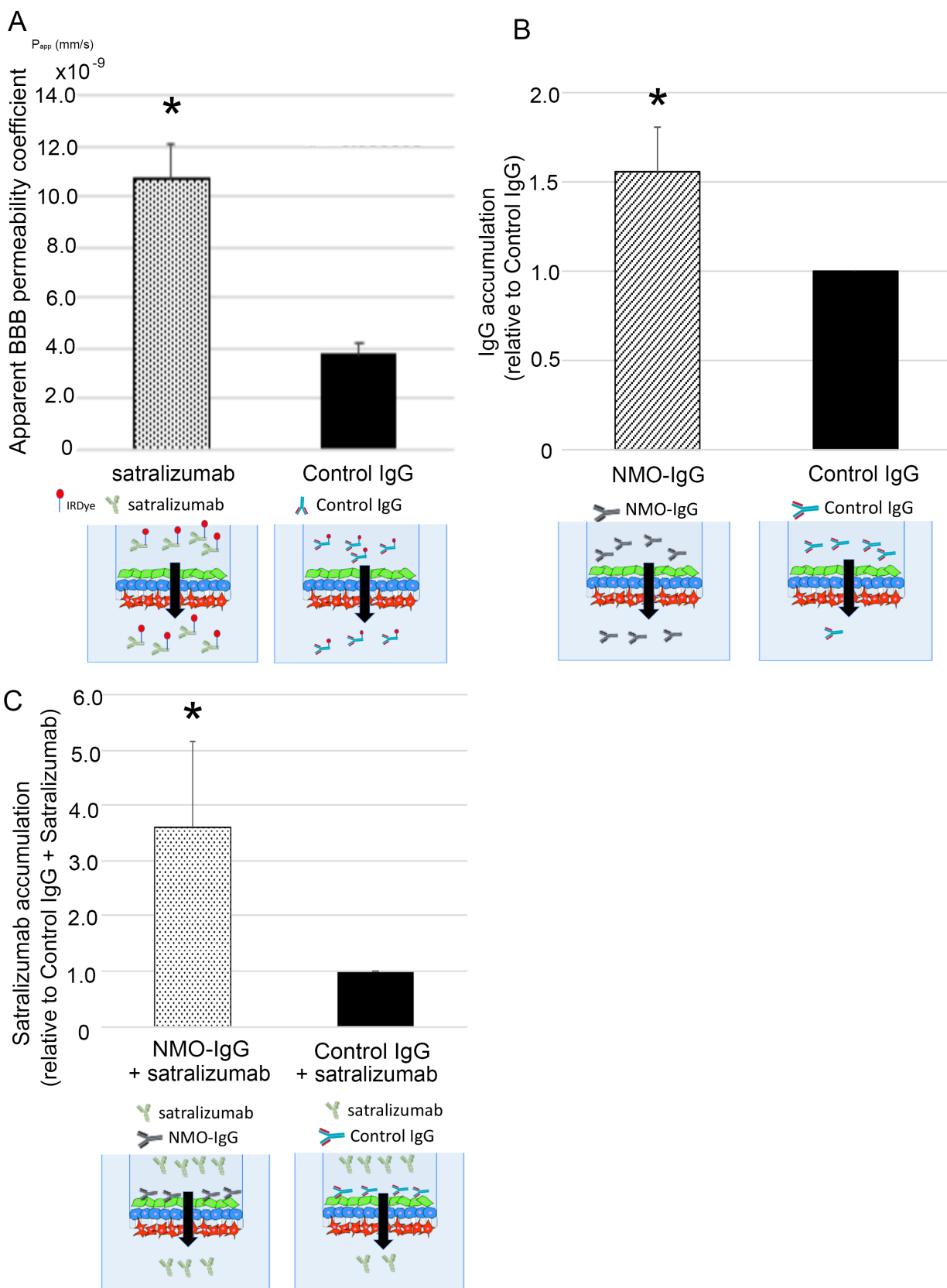
271

272 ***Intracerebral transferability of satralizumab in the presence of NMO-IgG in vitro***

273 To compare the microvolume translocation of satralizumab and NMO-IgG across the BBB with that of  
274 Control IgG, we constructed the *in vitro* BBB models in which measurement of microvolumes of satralizumab  
275 and IgG translocation through the BBB could be detected by Odyssey Infrared Imaging System and  
276 ELISA. We evaluated the apparent permeability coefficients of the BBB ( $P_{app}$ ; mm/s) with respect to  
277 satralizumab and Control IgG in a static *in vitro* BBB model. Labeled satralizumab or IgG2 (Control IgG) was  
278 added to the hEC (vascular) side. Then the IgG that was translocated to the brain parenchymal side was  
279 detected by an infrared imaging system, and the apparent BBB permeability coefficients for satralizumab and  
280 Control IgG were calculated. The  $P_{app}$  with respect to satralizumab was almost three times the  $P_{app}$  with respect  
281 to Control IgG (Fig. 7A).

282 After exposing the vascular side of the triple co-culture BBB model to NMO-IgG or Control IgG, the  
283 translocated IgG was detected by human IgG detection ELISA kit. The total amounts of accumulated IgG for  
284 NMO-IgG and Control IgG were calculated, normalized with respect to Control IgG, and reported as “IgG  
285 accumulation”. The intracerebral transferability of NMO-IgG was almost 1.5 times that of Control IgG (Fig.  
286 7B).

287 In a previous study, we found the transfer rate of MR16-1 across the BBB in EAE mice to be almost  
288 30 times that of normal mice (32). Thus, we explored whether the intracerebral transferability of satralizumab  
289 would be similarly increased in the presence of NMO-IgG. After exposing the vascular side of the triple co-  
290 culture BBB model to satralizumab plus NMO-IgG or to satralizumab plus Control IgG, the accumulated  
291 satralizumab was measured by ELISA with anti-satralizumab antibody. The total amount of satralizumab for  
292 “NMO-IgG plus satralizumab” was normalized with respect to “Control IgG plus satralizumab” and reported  
293 as “satralizumab accumulation”. The relative satralizumab accumulation for “NMO-IgG plus satralizumab”  
294 was significantly increased to almost three times that for “Control IgG plus satralizumab” (Fig. 7C).



296 **Figure 7.**

297 **Intracerebral transferability of satralizumab in the presence of NMO-IgG *in vitro*.**

298 **(A)** Analysis of microvolume IgG translocation through the BBB by the Odyssey Infrared Imaging System  
299 revealed that the BBB  $P_{app}$  for satralizumab was almost three times that for Control IgG. \* $P < 0.05$  by unpaired  
300 t-test ( $n = 6$  per group). **(B)** Analysis of microvolume IgG translocation through the BBB by the  
301 spectrophotometer revealed that the relative accumulation of IgG for NMO-IgG was almost 1.5 times that for  
302 Control IgG. \* $P < 0.05$  by unpaired t-test ( $n = 6$  per group). **(C)** ELISA with anti-satralizumab antibody  
303 showed that the relative accumulation of satralizumab for satralizumab + NMO-IgG was significantly  
304 increased to almost three times that for satralizumab + Control IgG. \* $P < 0.05$  by unpaired t-test ( $n = 8$  per  
305 group). All data are expressed as mean and SEM.

306

307 **Discussion**

308 Here, we successfully generated ideal *in vitro* and *in ex-vivo* BBB models for evaluating barrier function,  
309 leukocyte transmigration and intracerebral transferability of IgGs and satralizumab across the BBB utilizing  
310 the newly established triple co-culture system of temperature-sensitive conditionally immortalized human  
311 BBB cell lines (Fig.1). In *in vitro* studies, application of satralizumab to the vascular and brain parenchymal  
312 sides of the model suppressed the transmigration of total PBMCs and CD4<sup>+</sup> and CD8<sup>+</sup> cells, the transmigration  
313 of which was enhanced by NMO-IgG (Fig. 2). Then, we have shown that blockade of IL-6 signaling in EAE  
314 mice suppressed the migration of CD4-positive T cells into the spinal cord, prevented the increase in BBB  
315 permeability, and prevented the onset of myelitis (Fig. 3 and 6). In addition, NMO-IgG was found to cause  
316 significant barrier dysfunction, which was strongest when NMO-IgG was applied to both the vascular and  
317 brain parenchymal sides of the model; the effect was not as strong with application of NMO-IgG to the brain  
318 parenchymal side but it was stronger than with vascular application (Fig. 4). On the other hand, application of  
319 satralizumab inhibited NMO-IgG-induced barrier dysfunction; application of satralizumab to the vascular and  
320 brain parenchymal sides had the highest effect on inhibiting NMO-IgG-induced barrier dysfunction, while the  
321 effect of applying satralizumab to the brain parenchymal side was almost the same as with vascular application  
322 (Fig. 5). We also demonstrated that the intracerebral transferability of satralizumab was about three times that

323 of Control IgG and in the presence of NMO-IgG the intracerebral transferability of satralizumab was even  
324 further increased to more than that of NMO-IgG itself (Fig. 7).

325 In an earlier study into the pathophysiology of NMOSD at the BBB, we found that autoantibodies to  
326 GRP78 in NMO-IgG activate NF- $\kappa$ B signals in vascular endothelial cells and increase BBB permeability,  
327 leading to attack by NMO-IgG on astrocytes on the CNS side of the BBB (17). We also showed that NMO-  
328 IgG on the CNS side induces IL-6 expression in astrocytes and that IL-6 trans-signaling affects endothelial  
329 cells and modifies the properties of the BBB, including inducing the expression of several chemokines (CCL2  
330 and CXCL8) and decreasing the expression of claudin-5 as well as increasing the permeability with respect to  
331 solutes and increasing the transmigration of PBMCs (11). In the current study, we demonstrated that brain  
332 parenchymal application of NMO-IgG decreased the barrier function more strongly than did vascular  
333 application (Fig. 4), indicating that the reduction of barrier function by IL-6 signaling on the CNS side is much  
334 more than by NMO-IgG on the vascular side.

335 Therefore, with respect to the pathophysiology of NMOSD at the BBB, there appear to be several steps on  
336 both sides of the BBB involved in the onset of NMOSD (Fig. 8A). First, NMO-IgG (anti-GRP78 or an  
337 unknown antibody or antibodies) activates NF- $\kappa$ B signals in endothelial cells. Second, NMO-IgG decreases  
338 the barrier function on the vascular side. Third, NMO-IgG increases the intracerebral transferability of NMO-  
339 IgG itself. Fourth, NMO-IgG attacks the AQP4 of astrocytes and induces IL-6 expression in astrocytes. Fifth,  
340 IL-6 signaling affects endothelial cells on the CNS side. Sixth, IL-6 signaling more strongly decreases the  
341 barrier function on the CNS side than on the vascular side. Seventh, IL-6 signaling induces the expression of  
342 several chemokines (CCL2 and CXCL8) in endothelial cells. Eighth, the induced chemokines enhance  
343 infiltration of inflammatory cells. Finally, NMOSD develops.

344 To explore the action mechanism of satralizumab at the BBB in NMOSD, we evaluated the intracerebral  
345 transferability of satralizumab. Satralizumab was found to have potential intracerebral transferability almost  
346 three times that of Control IgG (Fig. 7A) and NMO-IgG was found to have intracerebral transferability almost  
347 1.5 times that of Control IgG (Fig. 7B). We then found that the intracerebral transferability of satralizumab in  
348 the presence of NMO-IgG was significantly increased to almost three times that in the presence of Control IgG

349 (Fig. 7C). These results mean that the intracerebral transferability of satralizumab is enhanced by NMO-IgG  
350 and that satralizumab can pass through the BBB and affect the CNS side.

351 We also demonstrated that satralizumab suppressed the decrease in barrier function induced by NMO-IgG  
352 (Fig. 5) and prevented NMO-IgG-induced enhancement of inflammatory cell infiltration (Fig. 2). In addition,  
353 administration of anti-IL-6 receptor antibody to mice at 1 week after induction of EAE prevented T cell  
354 migration and the development of EAE without inhibition of T cell differentiation (Fig. 3). Blockade of IL-6  
355 signaling suppressed the migration of CD4-positive T cells into the spinal cord, prevented the increase in BBB  
356 permeability, and prevented the onset of the myelitis in EAE mice.

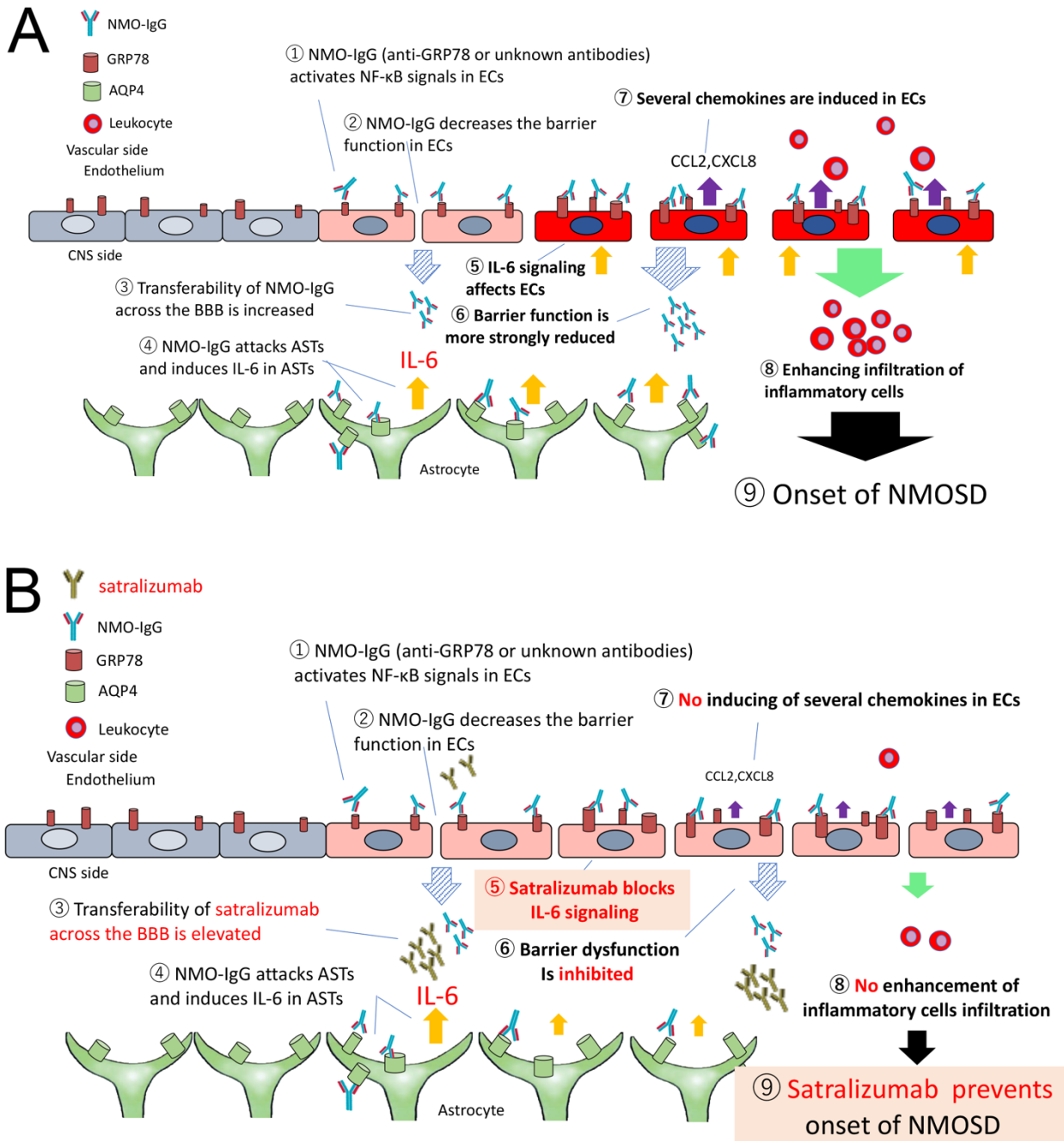
357 Consequently, with regard to the action mechanism of satralizumab at the BBB in NMOSD, it can be said  
358 that satralizumab can pass through the BBB in NMOSD and that blockade of IL-6 from astrocytes on the CNS  
359 side suppresses the BBB dysfunction and the induction of inflammatory cell infiltrates, leading to prevention  
360 of the onset of NMOSD (Fig. 8B). To be more specific, first, NMO-IgG (anti-GRP78 or an unknown antibody  
361 or antibodies) activates NF- $\kappa$ B signals in endothelial cells. Second, NMO-IgG decreases the barrier function  
362 on the vascular side. Third, NMO-IgG elevates the intracerebral transferability of satralizumab more than  
363 NMO-IgG. Fourth, NMO-IgG attacks the AQP4 of astrocytes and induces IL-6 expression in astrocytes. Fifth,  
364 satralizumab blocks IL-6 signaling on the CNS side. Sixth, blockade of IL-6 signaling by satralizumab inhibits  
365 the reduction of barrier function. Seventh, blockade of IL-6 signaling by satralizumab suppresses the  
366 expression of several chemokines (CCL2 and CXCL8) in endothelial cells. Eighth, satralizumab inhibits  
367 infiltration of inflammatory cells. Finally, satralizumab prevents the onset of NMOSD.

368 This study also indicated that the effect of satralizumab in inhibiting barrier dysfunction was almost the  
369 same with application to the brain parenchymal side as it was with application to the vascular side, although  
370 application to both the vascular and brain parenchymal sides had the highest inhibiting effect on barrier  
371 dysfunction (Fig. 5). On the other hand, our previous study (11) and the current study showed that the  
372 application of NMO-IgG to the vascular side did not induce leukocyte transmigration and, as a consequence,  
373 application of NMO-IgG plus satralizumab to the vascular did not show an inhibiting effect on leukocyte  
374 transmigration, although the application of NMO-IgG plus satralizumab (or IL-6 blockade) to the brain  
375 parenchymal side or to both sides strongly suppressed leukocyte transmigration. The reason for the differences

376 in barrier dysfunction and leukocyte transmigration seen between the vascular and CNS sides is still unsolved  
377 in this study. As regards the inhibiting effect on barrier dysfunction with application of satralizumab on the  
378 vascular side, we showed that sera from EAE mice mildly reduced the barrier function of endothelial cells in  
379 monoculture (Fig. S1). This result suggested that satralizumab (or IL-6 blockade) may directly or indirectly  
380 modify the barrier effect of endothelium on the vascular side.

381 We also showed that NMO-IgG increased the intracerebral transferability of satralizumab and IgG at the  
382 BBB. Because we previously found that NMO-IgG increased the permeability of the BBB with respect to  
383 solutes (11), the transportation of satralizumab might depend on this increased permeability. Recently, there  
384 have been several studies to identify determinants of the permeability-independent transport of  
385 immunoglobulin across the BBB (receptor-based endothelial transcytosis) (33–39). Several candidate  
386 molecules (transferrin receptor, insulin receptor, Fc-receptor of neonates [FCRN], and LDL receptor-related  
387 protein [LRR]) have been characterized and constitute the focus of ongoing research. In our experiments it is  
388 unresolved whether NMO-IgG increased the intracerebral transferability via permeability-dependent  
389 translocation or receptor-based endothelial transcytosis.

390 Because the therapeutic mechanisms of satralizumab at the BBB are as well-adapted for action in the acute  
391 phase of NMOSD by suppressing leukocyte migration as they are in the recurrence prevention period by  
392 inhibiting the barrier dysfunction, treatment with satralizumab is a promising strategy both to reduce the  
393 frequency of NMOSD attacks and to treat acute damage. Given the effect of satralizumab on BBB integrity, it  
394 may be a new option in the treatment of other conditions such as autoimmune optic neuritis and  
395 encephalomyelitis such as neuro-Behcet syndrome, CNS lupus, anti-NMDA receptor encephalitis, and Vogt-  
396 Koyanagi-Harada disease (40–42), all of which induce BBB breakdown and increase IL-6 concentration in the  
397 CSF.



399 **Figure 8**

400 **The pathophysiology of NMOSD at the BBB (A) and the action mechanism of satralizumab at the**  
401 **BBB (B). (A)** There are several steps on both sides of the BBB involved in the onset of NMOSD. First, NMO-  
402 IgG (anti-GRP78 or an unknown antibody or antibodies) activates NF- $\kappa$ B signals in endothelial cells (ECs).  
403 Second, NMO-IgG decreases the barrier function on the vascular side. Third, NMO-IgG increases the  
404 intracerebral transferability of NMO-IgG itself. Fourth, NMO-IgG attacks the AQP4 of astrocytes (ASTs) and  
405 induces IL-6 expression in astrocytes. Fifth, IL-6 signaling affects endothelial cells on the CNS side. Sixth, IL-  
406 6 signaling more strongly decreases the barrier function on the CNS side than on the vascular side. Seventh,  
407 IL-6 signaling induces the expression of several chemokines (CCL2 and CXCL8) in endothelial cells. Eight,  
408 the induced chemokines enhance infiltration of inflammatory cells. Finally, NMOSD develops. **(B)** First,  
409 NMO-IgG (anti-GRP78 or an unknown antibody or antibodies) activates NF- $\kappa$ B signals in endothelial cells.  
410 Second, NMO-IgG decreases the barrier function on the vascular side. Third, NMO-IgG elevates the  
411 intracerebral transferability of satralizumab more than NMO-IgG. Fourth, NMO-IgG attacks the AQP4 of  
412 astrocytes and induces IL-6 expression in astrocytes. Fifth, satralizumab blocks IL-6 signaling on the CNS  
413 side. Sixth, satralizumab inhibits the reduction in barrier function by blockade of IL-6 signaling. Seventh,  
414 blockade of IL-6 signaling by satralizumab suppresses the expression of several chemokines (CCL2 and  
415 CXCL8) in endothelial cells. Eight, satralizumab inhibits infiltration of inflammatory cells. Finally,  
416 satralizumab prevents the onset of NMOSD.

417 **Materials and Methods**

418 **Study design**

419 This was an experimental laboratory study designed to evaluate the effect of satralizumab on BBB disruption  
420 induced by NMO-IgG. This study used human IgG which was obtained from pooled serum collected from  
421 NMOSD patients and healthy volunteers.

422 First, we constructed a flow-based dynamic BBB model incorporating hEC/hPCT/hAST triple co-culture,  
423 and analyzed migrating cells by flow cytometry. Then we performed *in ex-vivo* experiments to evaluate the  
424 effect of anti-IL-6 receptor antibody on leukocyte migration into the spinal cords of EAE mice. In addition to  
425 *in vivo* assays, we evaluated the effect of satralizumab on NMO-IgG-induced transmigration of leukocytes in  
426 an *in vitro* BBB model.

427 Second, we evaluated whether NMO-IgG affected the barrier function, especially BBB permeability, of an  
428 *in vitro* BBB model incorporating hEC/hPCT/hAST triple co-culture. We also assessed the effect of  
429 satralizumab on BBB dysfunction induced by NMO-IgG. BBB permeability was evaluated by TEER values  
430 measured by an automated cell monitoring device. Then we performed *in vivo* experiments to evaluate the  
431 effect of anti-IL-6 receptor antibody on BBB permeability in EAE mice. BBB permeability *in vivo* was  
432 assessed by immunohistochemical analysis of spinal cords of mice. Furthermore, to assess the direct effect of  
433 the anti-IL-6 receptor antibody on BBB function, we evaluated the influence of anti-IL-6 receptor antibody on  
434 the permeability of a monolayer of mouse primary brain microvascular endothelial cells stimulated by serum  
435 from EAE mice.

436 Finally, we measured the intracerebral transferability of satralizumab *in vitro* by using ELISA and the  
437 Odyssey Infrared Imaging System. Figure legends indicate sample sizes and statistical tests used. For all  
438 *in vivo* experiments, subjects were randomly assigned to the experimental groups before experiments.

439 ***Human subjects***

440 The Institutional Review Boards of Yamaguchi University Graduate School of Medicine and Chugai  
441 Pharmaceutical Co., Ltd approved all study protocols, and signed informed consent was obtained from each  
442 blood donor.

443 ***NMO-IgG, Control IgG, and satralizumab***

444 NMO-IgG was the IgG fraction isolated from pooled serum collected from 10 patients with NMOSD, and  
445 Control IgG came from pooled serum collected from healthy volunteers at the Yamaguchi University Graduate  
446 School of Medicine. Both NMO-IgG and Control IgG were purified by protein G affinity and adjusted for  
447 assays by extensive dialysis. Satralizumab was prepared at Chugai Pharmaceutical Co., Ltd. We used NMO-  
448 IgG, Control IgG, and satralizumab at a final concentration of 100 µg/mL.

449 ***Cell culture***

450 Conditionally immortalized human microvascular endothelial cells (hECs; TY10), pericytes (hPCTs), and  
451 astrocytes (hASTs) were developed by transfection with temperature-sensitive SV40 large T antigen (ts-SV40-

452 LT). These cells proliferate at 33°C; at 37°C proliferation ceases and they differentiate into mature cells. hECs  
453 used were adult human brain microvascular endothelial cells transfected and immortalized with a plasmid  
454 expressing ts-SV40-LT as previously described (28, 29). hECs were grown in endothelial cell growth medium  
455 (EGM-2 Bulletkit; Lonza, Basel, Switzerland) supplemented with 10% fetal bovine serum (FBS), 100 U/mL  
456 penicillin (Sigma Aldrich, St. Louis, MO, USA), and 100 µg/mL streptomycin (Sigma Aldrich). hASTs were  
457 grown in Astrocyte Medium (ScienCell Research Laboratories, Carlsbad, CA, USA) containing 10% heat-  
458 inactivated FBS and 100 µg/mL streptomycin (Sigma Aldrich). hPCTs were maintained in Dulbecco's-  
459 modified Eagle's-medium (DMEM) (Gibco BRL) supplemented with 10% (v/v) heat-inactivated FBS and  
460 antibiotics (100 UI/mL penicillin G sodium, 100 µg/mL streptomycin sulfate). Astrocyte medium was used as  
461 the co-culture medium. All cells were maintained in 5% carbon dioxide at 33°C. All analyses were performed  
462 1 or 2 days after temperature was shifted from 33°C to 37°C.

463 ***Triple co-culture system***

464 hPCTs and hASTs were co-cultured on Transwell insert membranes having 3 µm pores (Corning Life  
465 Sciences, Tewksbury, MA, USA), with hPCTs on the luminal side and hASTs on the abluminal side. hECs  
466 were cultured in Nunc dishes with an UpCell surface (Thermo Fisher Scientific, Waltham, MA, USA), which  
467 afford sheet-like detachment of confluent cells and extra-cellular matrix when the temperature is shifted to  
468 20°C. The sheet of confluent hECs was detached and transferred onto the hPCTs co-cultured with hASTs on  
469 the insert. The polymers of the UpCell surface are slightly hydrophobic at 37°C but become hydrophilic at  
470 20°C to form an aqueous film between cells and polymers resulting in sheet-like detachment of cells including  
471 their surrounding native extracellular matrix structures.

472 ***Real-time monitoring system for TEER measurements with cellZscope***

473 The triple co-cultured inserts were transferred to an automated cell monitoring system (cellZscope; CellSeed  
474 Inc., Tokyo, Japan). After addition of satralizumab and NMO-IgG or Control IgG to the vascular (hEC) side or  
475 the brain parenchymal (hAST) side or to both sides, the TEER values were measured using the cellZscope  
476 device which can record the TEER every minute for 120 hours.

477 **PBMC isolation**

478 Peripheral blood mononuclear cells (PBMCs) were isolated from fresh heparinized blood of healthy subjects  
479 by density centrifugation with Lymphocyte Separation Medium (Mediatech, Herndon, VA, USA) as  
480 previously described (11), and used in transmigration assays within 2 hours of phlebotomy. For transmigration  
481 assays, PBMCs were resuspended at  $10 \times 10^6$  cells in 30 mL TEM buffer (RPMI 1640 without phenol red +  
482 1% bovine serum albumin + 25 mM HEPES) and stained with Calcein AM (Thermo Fisher Scientific) prior to  
483 perfusion into the 3D flow chamber device following the manufacturer's protocol (see below).

484 **Transmigration assay**

485 Flow-based transmigration assays were performed in a 3D Bioflux flow chamber device (Fluxion Bioscience,  
486 San Diego, CA, USA) as previously described (30). In brief, this system comprises a 3D flow pump, 3D flow  
487 chamber, and 3D flow membranes. The pump delivers a programmable shear flow over a wide range (0.1–  
488 200 dyne/cm<sup>2</sup>) to up to eight flow devices. The 3D flow chamber (width, 30 mm; length, 70 mm; height,  
489 8 mm) has three discrete reservoirs into which the 3D flow membranes fit completely. The 3D flow membrane  
490 is 8 mm in diameter and made of track-etched polycarbonate with 3  $\mu$ m pores. These membranes were coated  
491 with rat-tail collagen I solution (50  $\mu$ g/mL) (BD Biosciences, San Diego, CA, USA) and placed in a 12-well  
492 plate, whereupon hECs, hPCTs, and hASTs were triple co-cultured in Astrocyte Medium for 2 days at 33°C,  
493 after which time the membrane cultures were incubated for 1 day at 37°C. The membrane was gently  
494 transferred to the flow chamber, and  $10 \times 10^6$  PBMCs (total cells per assay) in 30 mL TEM (kept warm in a  
495 37°C water bath) were perfused via peristaltic pump through the chamber at a final concentration of  
496 333,000 cells/mL and at a shear stress of 1.5 dyne/cm<sup>2</sup> resulting in a total assay time of 60 minutes. All  
497 chambers were set on a 37°C slide warmer. After PBMC perfusion, the chamber was flushed for 5 minutes  
498 with phosphate-buffered saline (PBS) to remove loose cells, maintaining the same shear stress as in the assay.  
499 Migrated PBMCs were recovered from the bottom chamber. Cells that attached to the abluminal side of the  
500 membrane and the bottom chamber were removed by a quick rinse with 0.5 mM EDTA. The migrated cells  
501 were enumerated by a hemocytometer, then normalized to migrated cell numbers determined by flow  
502 cytometry. After collection, cells were fixed for 10 minutes in 1% paraformaldehyde at room temperature,

503 washed in PBS + 0.1 mM EDTA, followed by blocking in mouse IgG. Cells were labeled with anti-human  
504 CD45 efluor450, CD8a APC-efluor780 (eBiosciences, San Diego, CA, USA), CD3Alexa Fluor 647  
505 (BioLegend, San Diego, CA, USA), CD19 BV711, and CD4 PE-CF594 (BD Biosciences). Data were acquired  
506 using BD FACSCanto II (BD Biosciences), and analyzed by FlowJo software (v.10.4.1; Treestar, Ashland,  
507 OR, USA).

508 ***Measurement of microvolume IgG translocation by Odyssey Infrared Imaging System***

509 Control IgG and satralizumab were labeled with IRDye 800CW protein (IRDye 800CW Protein Labeling Kit;  
510 LI-COR, Lincoln, NE, USA) following the manufacturer's protocol. After exposing hECs in triple co-cultured  
511 inserts to labeled Control IgG or satralizumab, the microvolumes that translocated to the lower chamber were  
512 detected by an Odyssey Infrared Imaging System (LI-COR), and the apparent BBB permeability coefficient  
513 ( $P_{app}$ ; mm/s) was calculated from the degree of IgG translocation by using the following formula:

514 
$$P_{app} = V(dc/dt)/AC_0$$

515 where  $dc/dt$  = flux of IgG across the membrane;  $V$  ( $\text{cm}^3$ ) = volume on the receiving side;  $A$  ( $\text{cm}^2$ ) = surface  
516 area of insert; and  $C_0$  (mM) = initial concentration in the donor compartment.

517 ***Measurement of microvolume IgG translocation by spectrophotometer***

518 NMO-IgG or Control IgG were added to hECs in triple co-cultured inserts and incubated for 12 hours.  
519 Following the manual of the Easy-Titer Antibody Assay Kit (Thermo), anti-human IgG coated beads were  
520 added to the lower well and incubated with the sample for 60 minutes. Accumulated IgG in the lower well was  
521 measured by spectrophotometer, following the manufacturer's instructions. The total amount of accumulated  
522 IgG was normalized to 1 using Control IgG and reported as "IgG accumulation".

523 ***Measurement of microvolume satralizumab translocation by ELISA***

524 After exposing hECs in triple co-cultured inserts to satralizumab plus NMO-IgG or satralizumab plus  
525 Control IgG for 24 hours, the concentration of satralizumab in the lower chamber was measured by using  
526 ELISA with anti-satralizumab antibody. The samples were run in according to the manufacturer's protocol.

527 Total amount of accumulated satralizumab was normalized to 1 using “Control IgG + satralizumab” and  
528 reported as “Satralizumab accumulation”.

529 ***Animals***

530 Female C57BL/6J mice (7 weeks old; Charles River Laboratories Japan, Inc., Kanagawa, Japan) were used.  
531 All mice were fed ordinary laboratory chow and allowed free access to water under a constant light and dark  
532 cycle of 12 hours. All animal procedures were conducted in accordance with the Guidelines for the Care and  
533 Use of Laboratory Animals at Chugai Pharmaceutical Co., Ltd, and all experimental protocols were approved  
534 by the Animal Care Committee of the institution (approval No. 18-144, 19-191) and conformed to the *Guide*  
535 *for the Care and Use of Laboratory Animals* published by the US National Institutes of Health.

536 ***Experimental design of EAE mice***

537 Experimental autoimmune encephalomyelitis (EAE) was induced in mice by subcutaneous immunization (on  
538 Day 0) with 50 µg of the myelin oligodendrocyte glycoprotein 35–55 peptide (MOG35-55; Peptide  
539 International, Louisville, KY, USA) emulsified in complete Freund’s adjuvant (Difco Laboratories, Detroit,  
540 MI, USA) supplemented with Mycobacterium tuberculosis extract H37Ra (Difco Laboratories). In addition,  
541 mice received 250 ng pertussis toxin (List Biological Laboratories, Campbell, CA, USA) intravenously on Day  
542 0 and intraperitoneally on Day 2. Control mice were treated with complete Freund’s adjuvant and saline alone.  
543 Anti-IL-6 receptor antibody (MR16-1) was prepared using a hybridoma established in Chugai  
544 Pharmaceutical’s laboratories (43). The EAE mice were intraperitoneally administered MR16-1 (8 mg/mouse)  
545 on Day 7 after MOG35-55 immunization. On Day 15 or 16 after MOG35-55 immunization, spinal cords,  
546 spleens, and sera were harvested for immunohistochemistry, flow cytometry, and TEER studies.

547 ***Clinical score assessment***

548 EAE mice were sequentially scored for clinical signs of EAE according to the following scale: 0, no apparent  
549 disease; 1, limp tail; 2, hind limb weakness; 3, hind limb paresis; 4, hind limb paralysis; 5, hind limb and fore  
550 limb paralysis; 6, moribundity and death.

551 ***Immunohistochemistry***

552 Mice were anaesthetized with isoflurane, and transcardial perfusion was carried out with 20 mL of cold PBS.  
553 The L3–L5 segment of the lumbar spinal cord was removed, fixed in 4% paraformaldehyde, and placed in a  
554 30% sucrose solution overnight. Samples were embedded in optimal cutting temperature (OCT) compound,  
555 and frozen slices of spinal cord (10  $\mu$ m thick) were obtained with a cryostat. Spinal cord slices were stained by  
556 using the following primary antibodies: goat anti-albumin antibody (1:200, A90-134A; Bethyl Laboratories,  
557 Inc., Montgomery, TX, USA), biotin-conjugated donkey anti-mouse IgG antibody (1:200, 715-066-151;  
558 Jackson ImmunoResearch, West Grove, PA, USA), and rat anti-CD4 antibody (1:100, 550280; BD  
559 Pharmingen Inc., San Diego, CA, USA). After overnight incubation with primary antibodies at 4°C, spinal  
560 cord sections were incubated with secondary antibody Alexa Fluor 488-conjugated donkey anti-goat IgG  
561 (1:200, 705-546-147; Jackson ImmunoResearch) and Alexa Fluor 488-conjugated streptavidin (2  $\mu$ g/mL, 016-  
562 540-084; Jackson ImmunoResearch). For CD4 staining, biotin-conjugated donkey anti-rat IgG (1:200, 712-  
563 066-153; Jackson ImmunoResearch) and Alexa Fluor 488-conjugated streptavidin (2  $\mu$ g/mL, 016-540-084;  
564 Jackson ImmunoResearch) were used. Slides were mounted using Vectashield Antifade Mounting Medium  
565 (H-1200; Vector Laboratories, Burlingame, CA, USA). Spinal cord slices were randomly selected from each  
566 mouse and observed under a BZ-9000 Fluorescence Microscope (Keyence, Osaka, Japan). Positive-staining  
567 areas were calculated using BZ-II analyzer (Keyence) and CD4-positive T cells were counted with imaging  
568 analysis software (WinROOF Version 6.3.1; Mitani Corporation, Fukui, Japan)

569 ***Flow cytometry***

570 Spleens collected from Control mice and EAE mice were homogenized and passed through a 100 and 40  $\mu$ m  
571 cell strainer to isolate mononuclear cells. Red blood cells were hemolyzed with ACK lysing buffer (Gibco,  
572 Carlsbad, CA, USA). Mononuclear cells were incubated with Mouse BD Fc Block (BD Pharmingen Inc.)  
573 before staining. For intracellular cytokine staining, mononuclear cells were stimulated for 4 hours in RPMI  
574 1640 (Sigma, St. Louis, MO, USA) containing 10% FBS (Gibco), 55  $\mu$ M 2-mercaptoethanol (Gibco), 10 mM  
575 HEPES (Sigma), 1 mM sodium pyruvate (Wako, Osaka, Japan), and 100 U /mL penicillin-streptomycin  
576 (Gibco) with 50 ng/mL phorbol 12-myristate 13-acetate (Sigma) and 1  $\mu$ M ionomycin (Sigma) in the presence

577 of 0.1% BD GolgiPlug (BD Biosciences). The cells were initially stained with FITC-conjugated anti-CD4  
578 antibody (100510; BioLegend), and then intracellularly stained using PE-conjugated anti-IL-17A (506904;  
579 BioLegend), and APC-conjugated anti-IFN- $\gamma$  (505810; BioLegend) antibodies; staining was performed with  
580 the Fixation/Permeabilization Solution Kit with BD GolgiPlug (BD Biosciences) according to the  
581 manufacturer's protocol. For analysis of Treg cells, Fc-blocked cells were initially stained with FITC-  
582 conjugated anti-CD4 and BV421-conjugated anti-CD25 (102034; BioLegend) antibodies, and then  
583 intracellularly stained using the APC-conjugated anti-Foxp3 antibody (17-5773-80B; Invitrogen, Carlsbad,  
584 CA, USA); staining was performed with a Foxp3 Transcription Factor Staining Buffer Set (Invitrogen)  
585 according to the manufacturer's protocol. Data were acquired using BD FACSCanto II (BD Biosciences) and  
586 analyzed using FlowJo 10.4.1 (Treestar).

587 **Statistical analysis**

588 All data are expressed as mean and SEM. The statistical significance of differences was determined by using  
589 unpaired t-test, Tukey's multiple comparison test with ANOVA, or two-way ANOVA for comparison of time  
590 course data. Probability values of less than 0.05 were considered significant. Statistical analyses were  
591 performed using IBM SPSS Statistics (International Business Machines Corporation, Armonk, NY, USA) or  
592 JMP version 11.2.1 software (SAS Institute, Cary, NC, USA).

593 **Supplementary Materials**

594 Supplementary materials and methods  
595 Fig. S1. Effects of IL-6 receptor blockade on the barrier dysfunction induced by serum from EAE mice.

596 **References and Notes:**

597 1. A. Jacob, A. McKeon, I. Nakashima, D. K. Sato, L. Elsone, K. Fujihara, J. de Seze, Current concept of  
598 neuromyelitis optica (NMO) and NMO spectrum disorders. *J. Neurol. Neurosurg. Psychiatry* **84**, 922–930  
599 (2013).

600 2. D. M. Wingerchuk, B. Banwell, J. L. Bennett, P. Cabre, W. Carroll, T. Chitnis, J. de Seze, K. Fujihara, B.  
601 Greenberg, A. Jacob, S. Jarius, M. Lana-Peixoto, M. Levy, J. H. Simon, S. Tenembaum, A. L. Traboulsee,  
602 P. Waters, K. E. Wellik, B. G. Weinshenker, International Panel for NMO Diagnosis, International  
603 consensus diagnostic criteria for neuromyelitis optica spectrum disorders. *Neurology* **85**, 177–189 (2015).

604 3. V. A. Lennon, D. M. Wingerchuk, T. J. Kryzer, S. J. Pittock, C. F. Lucchinetti, K. Fujihara, I. Nakashima,  
605 B. G. Weinshenker, A serum autoantibody marker of neuromyelitis optica: distinction from multiple  
606 sclerosis. *Lancet* **364**, 2106–2112 (2004).

607 4. V. A. Lennon, T. J. Kryzer, S. J. Pittock, A. S. Verkman, S. R. Hinson, IgG marker of optic-spinal  
608 multiple sclerosis bind to the aquaporin-4 water channel. *J. Exp. Med.* **202**, 473–477 (2005).

609 5. S. Saadoun, P. Waters, B. A. Bell, A. Vincent, A. S. Verkman, M. C. Papadopoulos, Intra-cerebral  
610 injection of neuromyelitis optica immunoglobulin G and human complement produces neuromyelitis  
611 optica lesions in mice. *Brain* **133**, 349–361 (2010).

612 6. H. Zhang, J. L. Bennett, A. S. Verkman, Ex vivo spinal cord slice model of neuromyelitis optica reveals  
613 novel immunopathogenic mechanisms. *Ann. Neurol.* **70**, 943–954 (2011).

614 7. M. C. Papadopoulos, A. S. Verkman, Aquaporin 4 and neuromyelitis optica. *Lancet Neurol.* **11**, 535–544  
615 (2012).

616 8. M. Majed, J. P. Fryer, A. McKeon, V. A. Lennon, S. J. Pittock, Clinical utility of testing AQP4-IgG in  
617 CSF: Guidance for physicians. *Neurol. Neuroimmunol. Neuroinflamm.* **3**, e231 (2016).

618 9. F. Shimizu, Y. Sano, T. Takahashi, H. Haruki, K. Saito, M. Koga, T. Kanda, Sera from neuromyelitis  
619 optica patients disrupt the blood-brain barrier. *J. Neurol. Neurosurg. Psychiatry* **83**, 288–297 (2012).

620 10. B. Obermeier, R. Daneman, R. M. Ransohoff, Development, maintenance and disruption of the blood-  
621 brain barrier. *Nat. Med.* **19**, 1584–1596 (2013).

622 11. Y. Takeshita, B. Obermeier, A. C. Cotleur AC, S. F. Spampinato, F. Shimizu, E. Yamamoto, Y. Sano, T.  
623 J. Kryzer, V. A. Lennon, T. Kanda, R. M. Ransohoff, Effects of neuromyelitis optica-IgG at the blood-  
624 brain barrier in vitro. *Neurol. Neuroimmunol. Neuroinflamm.* **4**, e311 (2016).

625 12. T. Hosokawa, H. Nakajima, Y. Doi, M. Sugino, F. Kimura, T. Hanafusa, T. Takahashi, Increased serum  
626 matrix metalloproteinase-9 in neuromyelitis optica: implication of disruption of blood-brain barrier. *J.*  
627 *Neuroimmunol.* **236**, 81–86 (2011).

628 13. Y. Tomizawa, K. Yokoyama, S. Saiki, T. Takahashi, J. Matsuoka, N. Hattori, Blood-brain barrier  
629 disruption is more severe in neuromyelitis optica than in multiple sclerosis and correlates with clinical  
630 disability. *J. Int. Med. Res.* **40**, 1483–1491 (2012).

631 14. T. Matsushita, T. Tateishi, N. Isobe, T. Yonekawa, R. Yamasaki, D. Matsuse, H. Murai, J. Kira,  
632 Characteristic cerebrospinal fluid cytokine/chemokine profiles in neuromyelitis optica, relapsing remitting  
633 or primary progressive multiple sclerosis. *PLoS One* **8**, e61835 (2013).

634 15. A. Uzawa, M. Mori, M. Ito M, T. Uchida, S. Hayakawa, S. Masuda, S. Kuwabara, Markedly increased  
635 CSF interleukin-6 levels in neuromyelitis optica, but not in multiple sclerosis. *J. Neurol.* **256**, 2082–2084  
636 (2009).

637 16. A. Uzawa, M. Mori, K. Arai, Y. Sato, S. Hayakawa, S. Masuda, J. Taniguchi, S. Kuwabara, Cytokine and  
638 chemokine profiles in neuromyelitis optica: significance of interleukin-6. *Mult. Scler.* **16**, 1443–1452  
639 (2010).

640 17. F. Shimizu, K. L. Schaller, G. P. Owens, A. C. Cotleur, D. Kellner, Y. Takeshita, B. Obermeier, T. J.  
641 Kryzer, Y. Sano, T. Kanda, V. A. Lennon, R. M. Ransohoff, J. L. Bennett, Glucose-regulated protein 78  
642 autoantibody associates with blood-brain barrier disruption in neuromyelitis optica. *Sci. Transl. Med.* **9**,  
643 eaai9111 (2017).

644 18. N. Chihara, T. Aranami, W. Sato, Y. Miyazaki, S. Miyake, T. Okamoto, M. Ogawa, T. Toda, T.  
645 Yamamura, Interleukin 6 signaling promotes anti-aquaporin 4 autoantibody production from plasmablasts  
646 in neuromyelitis optica. *Proc. Natl. Acad. Sci. USA.* **108**, 3701–3706 (2011).

647 19. K. D. Rochfort, L. E. Collins, R. P. Murphy, P. M. Cummins, Downregulation of blood-brain barrier  
648 phenotype by proinflammatory cytokines involves NADPH oxidase-dependent ROS generation:  
649 consequences for interendothelial adherens and tight junctions. *PLoS One* **9**, e101815 (2014).

650 20. T. Uchida, M. Mori, A. Uzawa, H. Masuda, M. Muto, R. Ohtani, S. Kuwabara, Increased cerebrospinal  
651 fluid metalloproteinase-2 and interleukin-6 are associated with albumin quotient in neuromyelitis optica:  
652 Their possible role on blood-brain barrier disruption. *Mult. Scler.* **23**, 1072–1084 (2017).

653 21. M. Araki, T. Matsuoka, K. Miyamoto, S. Kusunoki, T. Okamoto, M. Murata, S. Miyake, T. Aranami, T.  
654 Yamamura, Efficacy of the anti-IL-6 receptor antibody tocilizumab in neuromyelitis optica: a pilot study.  
655 *Neurology* **82**, 1302–1306 (2014).

656 22. I. Ayzenberg, I. Kleiter, A. Schroder, K. Hellwig, A. Chan, T. Yamamura, R. Gold, Interleukin 6 receptor  
657 blockade in patients with neuromyelitis optica nonresponsive to anti-CD20 therapy. *JAMA Neurol.* **70**,  
658 394–397 (2013).

659 23. J. M. Reichert, Antibodies to watch in 2017. *Mabs* **9**, 167–181 (2017).

660 24. T. Igawa, S. Ishii, T. Tachibana, A. Maeda, Y. Higuchi, S. Shimaoka, C. Moriyama, T. Watanabe, R.  
661 Takubo, Y. Doi, T. Wakabayashi, A. Hayasaka, S. Kadono, T. Miyazaki, K. Haraya, Y. Sekimori, T.  
662 Kojima, Y. Nabuchi, Y. Aso, Y. Kawabe, K. Hattori, Antibody recycling by engineered pH-dependent  
663 antigen binding improves the duration of antigen neutralization. *Nat. Biotechnol.* **28**, 1203–1207 (2010).

664 25. T. Igawa, H. Tsunoda, T. Tachibana, A. Maeda, F. Mimoto, C. Moriyama, M. Nanami, Y. Sekimori, Y.  
665 Nabuchi, Y. Aso, K. Hattori, Reduced elimination of IgG antibodies by engineering the variable region.  
666 *Protein Eng. Des. Sel.* **23**, 385–392 (2010).

667 26. T. Yamamura, I. Kleiter, K. Fujihara, J. Palace, B. Greenberg, B. Zakrzewska-Pniewska, F. Patti, C. P.  
668 Tsai, A. Saiz, H. Yamazaki, Y. Kawata, P. Wright, J. de Seze, Trial of satralizumab in neuromyelitis  
669 optica spectrum disorder. *N. Engl. J. Med.* **381**, 2114–2124 (2019).

670 27. Y. Takeshita, R. M. Ransohoff, Inflammatory cell trafficking across the blood-brain barrier: chemokine  
671 regulation and in vitro models. *Immunol. Rev.* **248**, 228–239 (2012).

672 28. Y. Sano, F. Shimizu, M. Abe, T. Maeda, Y. Kashiwamura, S. Ohtsuki, T. Terasaki, M. Obinata, K.  
673 Kajiwara, M. Fujii, M. Suzuki, T. Kanda, Establishment of a new conditionally immortalized human brain  
674 microvascular endothelial cell line retaining an in vivo blood-brain barrier function. *J. Cell Physiol.* **225**,  
675 519–528 (2010).

676 29. F. Shimizu, Y. Sano, O. Tominaga, T. Maeda, M. Abe, T. Kanda, Advanced glycation end-products  
677 disrupt the blood-brain barrier by stimulating the release of transforming growth factor- $\beta$  by pericytes and  
678 vascular endothelial growth factor and matrix metalloproteinase-2 by endothelial cells in vitro. *Neurobiol.*  
679 *Aging* **34**, 1902–1912 (2013).

680 30. Y. Takeshita, B. Obermeier, A. Cotleur, Y. Sano, T. Kanda, R. M. Ransohoff, An in vitro blood-brain  
681 barrier model combining shear stress and endothelial cell/astrocyte co-culture. *J. Neurosci. Methods* **232**,  
682 165–172 (2014).

683 31. S. Man, B. Tucky, A. Cotleur, J. Drazba, Y. Takeshita, R. M. Ransohoff, CXCL12-induced monocyte-  
684 endothelial interactions promote lymphocyte transmigration across an in vitro blood-brain barrier. *Sci.*  
685 *Transl. Med.* **4**, 119ra14 (2012).

686 32. K. Serizawa, H. Tomizawa-Shinohara, M. Magi, K. Yogo, Y. Matsumoto, Anti-IL-6 receptor antibody  
687 improves pain symptoms in mice with experimental autoimmune encephalomyelitis. *J. Neuroimmunol.*  
688 **319**, 71–79 (2018).

689 33. U. Bickel, Y. S. Kang, T. Yoshikawa, W. M. Pardridge, In vivo demonstration of subcellular localization  
690 of anti-transferrin receptor monoclonal antibody-colloidal gold conjugate in brain capillary endothelium. *J.*  
691 *Histochem. Cytochem.* **42**, 1493–1497 (1994).

692 34. W. M. Pardridge, J. L. Buciak, P. M. Friden, Selective transport of an anti-transferrin receptor antibody  
693 through the blood-brain barrier in vivo. *J. Pharmacol. Exp. Ther.* **259**, 66–70 (1991).

694 35. Y. J. Yu, Y. Zhang, M. Kenrick, K. Hoyte, W. Luk, Y. Lu, J. Atwal, J. M. Elliott, S. Prabhu, R. J. Watts,  
695 M. S. Dennis, Boosting brain uptake of a therapeutic antibody by reducing its affinity for a transcytosis  
696 target. *Sci. Transl. Med.* **3**, 84ra44 (2011).

697 36. R. J. Boado, Y. Zhang, Y. Zhang, W. M. Pardridge, Humanization of anti-human insulin receptor antibody  
698 for drug targeting across the human blood-brain barrier. *Biotechnol. Bioeng.* **96**, 381–391 (2007).

699 37. W. M. Pardridge, Y. S. Kang, J. L. Buciak, J. Yang, Human insulin receptor monoclonal antibody  
700 undergoes high affinity binding to human brain capillaries in vitro and rapid transcytosis through the  
701 blood-brain barrier in vivo in the primate. *Pharm. Res.* **12**, 807–816 (1995).

702 38. G. Xiao, L. S. Gan, Receptor-mediated endocytosis and brain delivery of therapeutic biologics. *Int. J. Cell  
703 Biol.* **2013**, 703545 (2013).

704 39. D. P. Proulx, P. Rouleau, I. Pare, M. M. Vallieres-Noel, R. Bazin, Interaction between intravenous  
705 immunoglobulin (IVIg) and the low-density lipoprotein receptor-related protein 1: a role for transcytosis  
706 across the blood brain barrier? *J. Neuroimmunol.* **251**, 39–44 (2012).

707 40. P. Lin, Targeting interleukin-6 for noninfectious uveitis. *Clin. Ophthalmol.* **9**, 1697–1702 (2015).

708 41. T. Yoshimura, K. Sonoda, N. Ohguro, Y. Ohsugi, T. Ishibashi, D. J. Cua, T. Kobayashi, H. Yoshida, A.  
709 Yoshimura, Involvement of Th17 cells and the effect of anti-IL-6 therapy in autoimmune uveitis.  
710 *Rheumatology (Oxford)* **48**, 347–354 (2009).

711 42. T. Asano, H. Ito, Y. Kariya, K. Hoshi, A. Yoshihara, Y. Ugawa, H. Sekine, S. Hirohata, Y. Yamaguchi, S.  
712 Sato, H. Kobayashi, K. Migita, H. Ohira, Y. Hashimoto, H. Watanabe, Evaluation of blood-brain barrier  
713 function by quotient alpha2 macroglobulin and its relationship with interleukin-6 and complement  
714 component 3 levels in neuropsychiatric systemic lupus. *PLoS One* **12**, e0186414 (2017).

715 43. M. Okazaki, Y. Yamada, N. Nishimoto, K. Yoshizaki, M. Mihara, Characterization of anti-mouse  
716 interleukin-6 receptor antibody. *Immunol. Lett.* **84**, 231–240 (2002).

717

718 **Acknowledgments:** The authors thank Yoshihiro Matsumoto and Kenji Yogo of Chugai Pharmaceutical Co.,  
719 Ltd for ensuring the integrity of the *in vivo* study. **Funding:** This study was supported by research grants from  
720 Chugai Pharmaceutical Co., Ltd and from the Japan Society for the Promotion of Science (JSPS)  
721 (JP19K07975).

722 **Author contributions:** T.K. and R.M.R. conceptualized and designed the study. Y.T., S.F., and K.S. were  
723 involved in drafting the article. Y.T. performed real-time monitoring of TEER measurements with cellZscope.  
724 S.F. isolated PBMCs and conducted transmigration assays. Y.T. and K.M. constructed the triple co-culture  
725 system. S.F. and M.F. measured microvolume IgG and satralizumab. J.N., F.S., and Y.S. cultured the hECs,  
726 hPCTs, and hASTs and controlled the quality of these cell lines. K.S., H.T.-S., and S.M. were involved in data  
727 acquisition in EAE experiments. **Competing interests:** K.S., H.T.-S., and S.M. are paid employees of Chugai  
728 Pharmaceutical Co., Ltd. Chugai has filed a patent application related to the subject matter of this paper  
729 (PCT/JP2020/005965; Inhibitory effect of anti-IL-6 receptor antibody on BBB dysfunction). T.K. is a member  
730 of the advisory board of Chugai Pharmaceutical Co., Ltd. Y.T. and T.K. have filed a patent application related  
731 to the subject matter of this paper (WO2017179375A1, PCT/JP2017/011361; *In vitro* model for blood-brain  
732 barrier and method for producing *in vitro* model for blood-brain barrier). **Data and material availability:** All  
733 data associated with this study are present in the paper. hECs, hPCTs, and hASTs are available from T.K.  
734 under a material transfer agreement with the Yamaguchi University. MR16-1 is available under a material  
735 transfer agreement with Chugai Pharmaceutical Co., Ltd.

736

## 737 **Supplementary Materials**

### 738 **Materials and Methods**

#### 739 ***Transendothelial electrical resistance studies using mouse serum***

740 C57BL/6 Mouse Primary Brain Microvascular Endothelial Cells (BMECs, C57-6023; Cell Biologics Inc.,  
741 Chicago, IL, USA) were seeded on the upper (luminal) surface of culture well insert membranes. On the  
742 following day, cells were incubated with medium containing 10% serum from Control mice or EAE mice  
743 (clinical score  $\geq 1$ ). MR16-1 (100  $\mu$ g/mL) and soluble IL-6 receptor (100 ng/mL) were also added. After 1 day  
744 of incubation, TEER values were measured with Endohm-6 and EVOM2 (World Precision Instruments,  
745 Sarasota, FL, USA).